Science
AAAS

Supplementary Materials for

Climbing fiber multi-innervation of mouse Purkinje dendrites with arborization common to human

Silas E. Busch and Christian Hansel

Corresponding author: Christian Hansel, chansel@bsd.uchicago.edu

Science **381**, 420 (2023)
DOI: 10.1126/science.adi1024

The PDF file includes:

Other Supplementary Material for this manuscript includes the following:

Materials and Methods

Subjects

Human cerebellar tissue was collected from three embalmed donor bodies provided to the University of Chicago Pritzker School of Medicine Anatomy Lab by the Anatomical Gift Association of Illinois (AGAI). Individuals were 92 (F), 95 (F), and 86 (M) years old, died of causes unrelated to cerebellar morphology (e.g. 'failure to thrive', likely 'failure to thrive', and colon cancer, respectively), and tissue was stored for 2, 6, and 2 months, respectively. During life, all study subjects signed an informed consent approved by the AGAI.

For experiments involving mice, both *in vitro* and *in vivo*, all experimental and surgical procedures were in accordance with the University of Chicago Animal Care and Use Committee guidelines. We used wildtype C57BL/6J mice housed on a 12hr light/dark cycle. Animals of either sex were used in all experiments and no sex differences were observed in any reported measures.

Immunohistochemistry

Embalmed human tissue. Due to incomplete fixation during the embalming process, we immediately submerged whole cerebella in 4% paraformaldehyde (PFA) for one week after they were obtained. Following this fixation period, each specimen was sectioned by hand in the sagittal axis to obtain 2-5mm blocks from the mid-hemisphere of each individual. Given the anterior curvature of folia in the hemisphere, blocks were cut at varying angles relative to the midline. Tissue blocks with incomplete fixation of deep structures were further fixed for 2-4 days. Depending on their size, blocks were cut transversely into dorsal and ventral sections, typically through the horizontal fissure, such that Lobules III through VIIAf/Crus I were in the dorsal block and VIIAt/Crus II through VIIIB in the ventral block. Occasionally, we also needed to cut the dorsal block into rostral and caudal sections. Next, each block was rinsed in 0.01M Phosphate buffer saline (PBS), dried on one side, mounted with super glue into the slicing chamber of a vibratome (Leica VT-1000S), and sliced at 35µm in the parasagittal plane.

Slices selected for immunolabeling were transferred to a clear tray, placed over a broad-spectrum LED array, covered with a reflective aluminum foil lid, and photobleached at 4℃ for 3-4 days. This reduced the strong autofluorescence in the green channel. Then tissue was washed in 50mM Glycine in 0.01M PBS for 2hrs at 4℃ and incubated in 20mM Sodium Citrate in 0.01M PBS at 50-60℃ using a heated water bath for 30min. After cooling to room temperature (RT), tissue was washed in 20mM Sodium Citrate for 5min then rinsed 2x30sec in dH20. Next, slices were permeabilized at RT in 0.01M PBS containing 0.025% Triton-X (PBS-TX) for 1hr. Blocking was done with PBS-TX containing 5% normal donkey serum (NDS) and 5% bovine serum albumin (BSA) for 1hr at RT followed by incubation in guinea pig anti-calbindin primary antibody (1:1000; Synaptic Systems Cat# 214 004, RRID:AB_10550535) solution overnight (18-20hrs) at 4℃ with 1% normal donkey serum in PBS-TX. After 3x10min washes in PBS-TX at RT, slices were incubated in donkey anti-guinea pig AF488 secondary antibody (1:200; Jackson ImmunoResearch Labs Cat# 706-545-148, RRID:AB_2340472) for 2hrs at 4℃ with 1% NDS in PBS-TX. Finally, slices were washed in PBS-TX for 3x10min, mounted and coverslipped with Vectashield (Vector Laboratories, Inc.), and allowed to set overnight before visualization.

Slice reconstruction and cell counting. Slides were visualized under 10x or 20x magnification (Zeiss Achroplan 0.25NA, air; Olympus UMPlanFL N 0.5NA, water) and illuminated with an epi-fluorescent light source (LEJ HBO-100) cast through a 450nm-pass filter cube. This allowed us to manually scan through the cerebellar cortex and classify Purkinje cells (PCs) by their dendritic morphology and their location by foliar sub-region (e.g. gyrus, bank, and sulcus), both based on criteria listed below. Post-mortem storage, embalming, and subsequent short-term submersion in ethanol, which renders many antigen sites inaccessible, diminished the tissue quality; however, this provided some advantage for our purposes. The condition of the tissue resulted in a sparse labeling of PCs that we expect to be random and without morphological bias. The sparsity provided a clearer visualization of each cell's individual morphology and decreased the total number of cells so that an exhaustive count for each region was feasible and unbiased without the use of stereology.

To mark the morphology and cell location accurately in both human and mouse tissue, we initially traced the outlines of the pial surface, white matter tracts, and PC layer over low magnification images of the entire section. Cells were only included for categorization if the soma and at least 200µm lengths of primary dendritic trunks were clearly labeled such that all features of Normative, Split, and Poly categories were unambiguously present or absent (Fig. 1A and fig. S1; see criteria below). We marked the location and morphological type of each cell in the slice map and scanned these notes as an input image to a custom Matlab GUI where each point could be digitized. This allowed us to generate a .csv table output with a cell ID, XY coordinates, morphological category, foliar sub-region, and lobule of each marked cell (Fig. 1B and fig. S2). These data were imported to R for downstream analysis and plotting.

Purkinje cell morphological category definitions and criteria. In human, PCs were deemed Normative if they had the following features: 1) a single trunk emerging from the soma, and 2) either no bifurcation of the primary trunk within two soma distances (2x the diameter of the soma, 25-35µm per soma) or a highly asymmetrical bifurcation where the smaller branch did not project in the parasagittal axis more than 200µm from the main dendritic compartment. PCs were defined as Split if they had the following features: 1) a single trunk emerging from the soma, and 2) either symmetrical bifurcation of the primary trunk within two soma distances or an asymmetrical bifurcation within two soma distances where the smaller branch projected more than 200µm from the main dendritic compartment and thus reached prominence by its overall length and sub-branching. PCs were defined as Poly if they had more than one trunk emerging from the soma regardless of relative size.

In mouse, PC categories were defined the same way, except that the bifurcation threshold of two soma distances (each soma diameter is 18-22µm) was set at 40µm, and the smaller branch of an asymmetrical bifurcation had to project only 100µm away from the main dendritic compartment.

In mouse and human, Split and Poly PCs were further subdivided into Vertical or Horizontal ramification patterns (fig S4B). Split and Poly PCs were defined as Horizontal if one of two primary dendrites ramified parallel with the PC layer for >300µm in human (>150µm in mouse), or both primary dendrites ramified in opposing directions parallel with the PC layer for >150µm each in human (>75µm in mouse). Dendrites were considered parallel if dendrite, at 300 or 150µm from the soma respectively, ramified at <30º from the top of the PC layer. Otherwise, the cell was defined as Vertical.

Foliar sub-region category definitions and criteria. Purkinje cell locations were defined as either Gyrus, Bank, or Sulcus based on the relative expansion/compression of the granule cell/molecular layers in the parasagittal axis (fig S4A). *Gyrus* was defined as a region where the total parasagittal length of the pial surface exceeded that of the border between the granule cell layer and the white matter. *Bank* was defined as regions where those two lengths were equal, such that neither layer of the cortex was compressed or expanded relative to the other. Finally, *Sulcus* was defined as regions where the total parasagittal length of the pial surface was less than that of the border between the granule cell layer and the white matter. Both intermediate sulci, embedded within a continuous Bank region, and full sulci were combined for these analyses.

Climbing fiber tracer immunohistochemistry. Tracer injections in the inferior olive (Fig. 2A) were performed on mice aged 13-15 weeks under ketamine/xylazine anesthesia (100 and 10mg/kg, respectively, 0.1mL/10g weight, Covetrus) with subcutaneous injections of meloxicam (0.06mL, 1-2 mg/kg), buprenorphine (0.05mL, 0.1 mg/kg, Covetrus), and sterile saline (0.5-1mL). Body temperature was maintained at 35-37℃ with a feedback dependent heating pad. Mice were positioned in an upright, sitting position with the head clamped such that the line described by the maxilla and the ear bars in the acoustic foramen was parallel with ground. In this configuration, the atlanto-occipital joint membrane was exposed when skin above the posterior skull and posterior muscles attaching to the occipital bone were removed. Cutting open the membrane, approximately 1uL of 25% Alexa 594 conjugated dextran amine tracer (10,000 MW, Invitrogen) in saline was injected 1.8mm deep and 0.5mm lateral from midline into the medulla at a 59º angle (30). After 4-5 days of recovery, mice were anesthetized with ketamine/xylazine (100 and 10mg/kg) and perfused with 4% PFA. Cerebella were removed and incubated for 2hrs in 4% PFA at 4℃ and then overnight in 30% sucrose in 0.1M PB at 4℃ (until the tissue sank from the surface). The tissue was then rinsed briefly in 0.1M PB, dried and blocked, submerged in OCT medium, flash frozen, and then sliced (50µm, parasagittal plane) using a cryostat microtome (CM 3050S, Leica).

After slicing, tissue was immunolabeled as described above with several changes: glycine incubation for 1hr instead of 2hrs and heated Sodium Citrate incubation for 20min instead of 30min. Slices were incubated in primary antibody solution with rabbit anti-VGluT2 (1:500; Thermo Fisher Scientific Cat# 42-7800, RRID:AB_2533537) and guinea pig anti-calbindin (1:1000), then in secondary antibodies with donkey anti-rabbit AF647 (Jackson ImmunoResearch Labs Cat# 711-605-152, RRID:AB_2492288) and donkey anti-guinea pig AF488 (both 1:200). Slices were imaged at 40x (Zeiss EC Plan-Neofluar 1.3NA, oil immersion) and z-stacks of the molecular layer were obtained with a confocal microscope (Fig. 2B; Zeiss LSM 5 Exciter, Axioskop 2).

Aldolase-C/Zebrin II immunohistochemistry and quantification. Human and mouse tissue was immunolabeled as described above for each respective species. For double immunolabeling in human, unembalmed tissue was obtained after storage at 4℃ for two days post-mortem, fixed in 4% PFA for 5 days, and sliced as described above for embalmed tissue. Slices were incubated first in primary antibody solution with mouse anti-Aldolase-C (i.e. zebrin II; 1:500; Santa Cruz Biotechnology Cat# sc-271593, RRID:AB_10659113) and guinea pig anti-calbindin (1:500), then in secondary antibodies with donkey anti-mouse AF488 (Jackson ImmunoResearch Labs Cat# 715-545-150, RRID:AB_2340846) and donkey anti-guinea pig AFCy3 (both 1:200; Jackson ImmunoResearch Labs Cat# 706-165-148, RRID:AB_2340460). Within each species,

imaging parameters were consistent across images to allow comparison of expression intensity (fig S3A and D).
In mouse, a series of z-stack images were collected at 40x (Zeiss EC Plan-Neofluar 1.3NA, oil immersion) in representative regions of dorsal anterior and posterior lobules with a confocal microscope (Zeiss LSM 900, Examiner.Z1). Cells were classified as either Zebrin+ or Zebrin- (Fig. S3A) and the location and cellular morphology was noted (fig S3B and C). In human, a series of images were collected at 10x (Zeiss Achroplan 0.25NA, air) in representative regions of lobules VII and VII in the hemisphere and lobules III-VIII in the vermis. Each image had ~15-20 visible somas, of which typically half of the cells were complete enough to allow morphological categorization. Somatic compartment ROIs were drawn manually in ImageJ and the mean intensity of both calbindin and zebrin II as well as cellular morphology was noted for each cell. Due to more variable cell quality in human compared to mouse tissue, we used the expression of calbindin, a universally expressed protein in Purkinje cells, as a baseline to normalize zebrin II intensity by subtracting calbindin intensity from zebrin II intensity and dividing by calbindin intensity. We then categorized cells in either the top or bottom 25th percentiles as Zebrin+ or Zebrin- (fig S3E).

Slice Electrophysiology

To quantify the frequency of functional climbing fiber (CF) multi-innervation, we used whole cell patch clamp and electrical stimulation in acute cerebellar slices with a cesium internal solution. Mice (P20-65) were anesthetized with isoflurane and decapitated. The cerebellum was immediately dissected in ice cold artificial cerebrospinal fluid (ACSF) containing (in mM): 124 NaCl, 5 KCl, 1.25 Na_2HPO_4, 2 $CaCl_2$, 2 $MgSO_4$, 26 $NaHCO_3$, and 10 D-glucose, bubbled with 95% O_2 and 5% CO_2. Sagittal slices of the cerebellum (250μm thick, including medial hemisphere, paravermis, and vermis) were prepared with ice cold ACSF in a chilled slicing chamber using a vibratome (Leica VT-1000S), and allowed to recover for 1hr at room temperature in oxygenated ACSF. During recordings, the slices were continuously perfused with oxygenated ACSF containing 100μM picrotoxin to block $GABA_A$ receptors.

Whole cell patch-clamp recordings from the PC somata were performed at room temperature using an EPC-10 amplifier (Fig. 2C and S3A; HEKA Electronics). The workstation was also equipped with a confocal microscope (Fig. 2C; LSM 5 Exciter and Axioskop 2, Zeiss) for the identification and morphological characterization of patched and dye-filled cells. Currents were filtered at 3kHz, digitized at 25kHz, and acquired using Patchmaster software (HEKA Electronics). For recordings of CF-EPSCs (Fig. 2C and S3A-B), the pipette solution was Cesium based to improve space clamp of inputs to distal dendrites and contained (in mM): 60 CsCl, 10 Cs D-Gluconate, 20 TEA-Cl, 20 BAPTA, 4 $MgCl_2$, 4 Na_2ATP, 0.4 Na_3GTP, 30 HEPES (osmolarity: 295-305mmol/kg; pH 7.3, adjusted with CsOH). Alexa-633 dye (30μM) was added to the pipette solution to allow visualization of the dendritic arbor. Pipette solution was kept on ice and shielded from light during the experiment to prevent degradation of the dye or ATP and GTP salts. Patch pipettes had a tip resistance of 4-6MOhm and were mounted in a motorized manipulator (Luigs & Neumann). Liquid junction potential was not corrected. Fast and slow capacitances were compensated, and series resistance was partially compensated (50-80%). Cell health was monitored through the consistency of input current and by calculating series and input resistances with test pulses throughout the recording (fig. S5B). Cells were rejected if any value deviated ±20% of baseline for more than 1min.

CF inputs were stimulated with 0.2ms step pulses using an electrode connected to an isolated current source (SIU91A, Cygnus Technology) and immersed in a glass pipette filled with ACSF. The cell was held in voltage clamp at -10 to -30mV. The stimulus intensity (0-150nA) and location (2-4 sites in the granule cell layer, 50-150μm from the PC soma, spanning the space sub-adjacent to the dendritic arbor) were systematically varied to search for multiple CF inputs. CF excitatory post-synaptic currents (EPSCs), particularly of reduced amplitude in some multi-innervated cells, were distinguished from parallel fiber (PF)-EPSCs by their paired pulse depression (400ms interval) and stable amplitude with small changes in stimulus intensity. PF-EPSCs exhibit paired pulse facilitation and linear amplitude relationship with even small stimulus intensity changes due to the recruitment of additional fibers.

CF-EPSCs were recorded after 20min post-patch to allow sufficient perfusion of cesium and dye. CF multi-innervation was only determined with multiple, discrete and consistent EPSC amplitude steps during both increasing and then decreasing stimulus intensity. After each recording, confocal z-stack images of each cell were obtained with a 63x objective (EC Plan-Neofluar 1.3NA, water immersion, Zeiss) using Zen software.

Two-Photon Ca^{2+} Imaging

Cranial window and GCaMP injection surgeries. Surgeries were performed on animals aged 10-12 weeks under ketamine/xylazine anesthesia (100 and 10mg/kg) with subcutaneous injections of meloxicam (1-2 mg/kg), buprenorphine (0.1 mg/kg), and sterile saline (0.5-1mL) as above. Body temperature was maintained at 35-37°C with a feedback dependent heating pad. The skin above the posterior skull was excised and the bone cleaned to implant a metal headframe over the interparietal bone via dental cement. After 3-4 days of recovery, mice were anesthetized and a 4mm craniotomy and durectomy was made at 2.5mm lateral from midline and 2.5mm caudal from lambda, exposing cerebellar simplex, crus I, and anterior crus II. A glass microelectrode with ~300μm tip diameter was used to inject a viral cocktail with low titer PC-specific L7-Cre (0.5%, AAV1.sL7.Cre.HA.WPRE.hGH.pA; Princeton Neuroscience Institute (PNI) Viral Core Facility; acquired from the lab of Dr. Samuel Wang, Princeton University) and high titer Cre-dependent GCaMP6f (20%, AAV.CAG.Flex.GCaMP6f.WPRE.SV40; Addgene, #100835) was injected ~300μm below the pial surface of medial and/or lateral crus I (~900nL per site, 5min wait before needle retraction) and a two-layer cranial window (4mm inner window, Tower Optical; 5mm outer window, Warner Instruments) was implanted over the craniotomy and sealed with dental cement (Metabond).

Habituation. The mice recovered for 7 days before habituation began. During the first week, habituation sessions were conducted every other day and consisted of exposure to handling and then to the imaging apparatus and head fixation on the treadmill. In the last 3 days before the experiment (6-10 days after habituation began), mice were habituated every day to head fixation, noises and activity typical during an experimental session, and occasional exposure to multisensory stimuli. Habituation allowed animals to exhibit relative comfort and reduced running behavior.

Imaging protocols. Imaging experiments were performed when the GCaMP6f indicator reached stable expression in a sparse cell population (11-20 days post-injection). PC dendrites were imaged at either 61.8 or 30.9Hz using a laser scanning two-photon microscope (Mai Tai DeepSee, Spectra-Physics) with an 8KHz resonant scanning module (Thorlabs) and 16x water

immersion objective (Nikon LWD 0.8NA, 3mm WD) controlled with Scanbox (Neurolabware). A digital 4x magnification was used for imaging lateral crus I during spontaneous and multisensory experiments and 2x for imaging medial crus I during whisker stimulation experiments. GCaMP6f was excited using a 920nm femtosecond-pulsed two-photon laser (~30mW laser power at sample; Spectra-Physics) and fluorescence emission collected by a GaAsP PMT (Hamamatsu). Interlocking light shields were fit around the headframe and objective to block ambient light from increasing background noise and to prevent an artifact from blue light stimuli directed at the eye. The microscope is custom designed with a rotating objective turret such that the angle of imaging could be adjusted to capture a perpendicular cross-section of PC dendritic arbors, thus reducing each cell's imaging profile to reduce the chance of contamination.

In order to increase the imaging rate for spontaneous and multisensory experiments to 62Hz, a narrow field of view was used (656 x 256 pixels scanned instead of 656 x 512 lines for whisker experiments). To image the complete arbor of several PCs when the short axis of the field of view was only ~153µm, we installed the treadmill, camera, and stimulus apparatuses on a large rotating platform (Thorlabs) such that the animal and all experimental components could be rotated under the objective until the parasagittal plane of PC dendrites aligned with the long axis (~392µm) of the image. Having the entire width of the dendrites aligned with the scanning direction also provided the benefit of technically optimizing the scanning time for each cell, thus reducing the chance for movement artifacts to appear as a branch-specific signal.

Volumetric imaging to confirm morphology. At the end of each imaging session, a volumetric scan was performed over the field of view at the maximum z-resolution of 2µm per step. For each scan, the laser power was turned up to 4-15%, the PMT gain down to 0.7-0.85, and 20-30 images were collected and averaged per step for optimal spatial resolution and morphological detail. Cells were only accepted for use if the somatic and dendritic compartments were entirely visible and major branch points of the primary dendrite were differentiable. These rules restricted our analyses to cells wherein the following parameters were unambiguous: 1) distance from the soma to primary dendrite split, 2) presence or absence of multiple primary trunks emerging from the soma, 3) rostral-caudal distance between branch centroids, and 4) maximal rostral-caudal spread of the whole dendritic arbor. For high-magnification recordings at 4x zoom, where multiple regions of interest (ROIs) were drawn for each major dendritic branch (spontaneous and multisensory experiments), we additionally required the unambiguous distinction of lesser branch points generating sub-compartments. Each cell's dendritic measurements and morphological category were noted at this time.

Stimulus Conditions

Multisensory stimuli. During each experiment, calcium activity was monitored in ~1-10 cells per animal during 20s imaging sessions. One of eight stimulus types (1. Light, 2. Air Puff, 3. Sound, 4. Light + Puff, 5. Light + Sound, 6. Puff + Sound, 7. Light + Puff + Sound, and 8. Control without stimulus) was triggered 10s after scanning initiation and lasted for 30ms. Light stimulus was a 488nm LED light (Prizmatix) targeted to the ipsilateral eye, Air Puff was delivered at 10psi (Picospritzer III, Parker Hannifin) via a 0.86mm diameter capillary tube positioned 2-3mm from the center of the ipsilateral whisker pad, and Sound stimulus was a 12kHz pure tone produced by speakers (Harman/Kardon) positioned bilaterally at ~70-80dB. The stimuli were applied with inter-stimulus intervals ≥ 30s. An Arduino Uno microcontroller

triggered by the imaging software provided distinct stimulus type triggering output to the light, puff, and tone instruments. The microcontroller was programmed to cycle through stimulus types randomly until 15 trials were acquired of each type (120 trials total).

Spontaneous activity. Spontaneous activity was obtained either on a day without sensory stimulation, or from the 10s pre-stimulus baseline period of multisensory imaging sessions. Trials were only used if the animal was resting such that there was no active running and/or whisking (*63*).

Single whisker stimulation. We obtained a sparse expression of GCaMP6f in PC dendrites and habituated mice to head fixation as described above. In some cases, we used the same mice for this experiment after spontaneous recordings were collected. Before the experiment began, we identified whisker responsive areas of medial Crus I by gently brushing varying numbers of whiskers and observing cellular activity in real time. We then sedated the animals with a minimal dose of ketamine/xylazine (80 and 8mg/kg, respectively) before headfixing them at the two-photon microscope. We strived to conduct the experiment during the 40-60min that the animal was in a stable level of sedation, so whisker responses and spontaneous activity were as close to comparable across whiskers and animals as possible. In a few cases a supplemental dose was required; the experiment was paused while the animal was waking, receiving the supplement, and returning to an equivalent state of sedation.

When the animal reached a state of anesthesia where it stopped actively whisking, a glass capillary tube attached to a rotating motor (SG92R Micro servo, Tower Pro) was manually manipulated to capture a single whisker. Previous work has shown that CF-dependent complex spike responses to whisker stimulation are most commonly tuned to dorsal, caudal, and dorso-caudal directions of whisker displacement (45), so the rotating servo was oriented such that rotation moved the whisker at 135º in the dorsal-caudal direction (fig S8A).

It is important to note that these experiments are meant as a proof of principle which cannot be construed to represent naturalistic behavior in the awake animal. As previously reported (46), responses to whisker stimulation, particularly of a single whisker, are very sparse in the anesthetized animal (~10% of trials). Several approaches could be used to compensate for this. Most obviously, experiments could be conducted in the awake animal when responsiveness is elevated. This approach did not work for us as it is virtually impossible to isolate a single whisker in a capillary tube while the mouse is awake (even if all but some whiskers are trimmed, which we prefer to avoid), and it would be extremely challenging to segregate active whisking from experimental passive whisker deflection. Second, while the animal is under anesthesia numerous individual trials (perhaps 50) with distant stimulus times could be conducted on a single whisker to confidently identify a response that is distinct from spontaneous CF activity. While this approach is more attractive for several reasons, it poses a substantial logistical problem as it would require a long time (>30min) to test a single whisker. This substantially limits how many whiskers could be tested under a consistent state of anesthesia, which massively reduces the chances of identifying whisker responses. Given the limitations of these approaches, we designed an experimentally bootstrapped stimulus wherein each whisker was stimulated many times at a high rate. At the expense of a possible change in responsiveness with repeated stimuli, this allowed many attempts to produce a response, while accelerating our recordings so we could test a large set of whiskers in each animal.

The servo was controlled by an Arduino Uno microcontroller programed to execute a sine function (7º maximal rotation forming an arc circumference of ~1.5cm at the tip of the capillary tube) at a rate of 2Hz for 50s (100 total stimulations of the whisker with 500ms intervals between starting movement initiations). The microcontroller was triggered by the imaging software with a 10s delay-to-start so spontaneous activity was recorded of ahead of each whisker stimulation. Images were thus 60s in duration (10s spontaneous activity and a 50s stimulation epoch), and two trials were conducted per whisker (200 total stimulations with 20s of spontaneous recording). After two trials, the capillary tube was manually withdrawn and moved to another whisker. Across animals, seven whiskers were stimulated in random order (β, γ, C1, C2, C3, B2, D2; occasionally D1 if D2 was inaccessible).

To sample a wider population of cells and increase the chance of observing whisker responses, imaging was conducted at 2x digital magnification and 31Hz, rather than 4x and 62Hz as above. As in previous 2-photon experiments, a z-stack was obtained at the end of recording to measure morphological properties of each cell and allow ROIs to be drawn manually across dendrites.

Two-photon image processing

Images were converted to tiffs and motion corrected using custom MATLAB scripts. Cellular ROIs were drawn manually in ImageJ based on volumetric cell reconstructions. The plane of focus for each experiment was selected to maximize the dendritic area of each branch of each target PC present in the scan while remaining within the intermediate region of the molecular layer. As a result, most interbranch ROIs were reasonably similar in size (representative example ROIs can be observed in Fig. 3B and D, Fig. 4A, and Fig. 5A), and there was no systematic difference in the ratio of interbranch ROI areas by morphological type. In unusual cases where there were substantial differences (>10:1) in size or profile of branches within the imaging plane, the cell was removed from consideration if the smaller ROI exhibited a higher baseline noise level. Another MATLAB script measured the pixel intensity of each ROI across frames and videos and saved the data as a .mat file. An interactive MATLAB GUI was used to manually confirm detection quality and consistency across imaging sessions to either include or exclude each cell for downstream analysis. Analyses were performed using MATLAB scripts and output for final data shaping, plotting, and statistics in R.

Manual event curation. In preliminary experiments, an interactive MATLAB GUI was used to manually curate a findpeaks autodetection of events. Curation involved adjusting rise and peak times as needed and, in cases of a branch-specific event, marking trace locations where a peak was missing. Thus, missed events could be tallied to obtain the number of local events (fig S7A).

Calcium peak detection and comparing inter-branch signals. Raw signal from all ROIs was imported to a custom MATLAB script that performed a five-frame moving window smoothing function and a background correction function. Then, ROI traces were input to the MATLAB version of OASIS deconvolution to obtain times and amplitudes of calcium peaks exceeding 3SD of the baseline. We decided not to distinguish between multiple tightly clustered events producing a single, accumulated large amplitude peak. While accumulated peaks from clustered inputs often retain multiple peaks (a partial peak within the rising phase of the larger event), the slow time constant of the GCaMP6f indicator and the natural variability between small, branch

ROIs can alter the appearance of multiple peaks and produce varying spike deconvolutions. This reduces our confidence in the ability to appropriately determine if there is a branch-specific event within a cluster of global events. As such, we identified peak times <4 frames apart – having only 1-2 frames (16-32ms) between detected peaks, which is below the ~50ms rise time constant of GCaMP6f (*64*) – and took only the second and highest peak or the last in a sequence of >2 events all of which are <4 frames apart.

To compare the deconvolved signal of each branch within a cell, we segregated the data for each trace into five groups: all signal in branch 1, all signal in branch 2, only global events, only local events in branch 1, and only local events in branch 2. Branch number assignment was arbitrary. Subsequent analyses were then performed on each subset of detected peaks individually.

Whisker movement traces and timing. First, whisker stimulation times were obtained from 30Hz video recordings (Genie Dalsa, Phase 1 Technology) of the mouse face where the stimulated whisker and the capillary tube moving the whisker were clearly visible. An ROI was drawn in ImageJ at the location in the capillary tube's movement trajectory where the whisker started to be bent or translated. Thus, when the whisker was moved, the bright capillary tube passed through the ROI and created a time locked peak in light intensity. The entire trace for each video (1min) was extracted in ImageJ for downstream analyses in a custom MATLAB script.

The first derivative of pixel intensity across frames was calculated for each trace, a baseline was measured during the 10s spontaneous period where there was no whisker movement, and whisker stimulus onset times were thus identified as the n-1 frame where a peak in the first derivative exceeded 3SD of the baseline. This also captured the return movement of the capillary tube that returned the whisker to its natural position.

Whisker experiment calcium signal. The same methods as described above were used to obtain calcium signal traces from two-photon recordings. Raw signal from all ROIs was imported to a custom MATLAB script that performed the same smoothing and background correction as described above. Then, ROI signals for each cell were analyzed two ways: averaged into a whole cell signal trace or kept separate to independently assess each branch. We input either whole cell or branch traces into OASIS deconvolution to obtain times and amplitudes of calcium peaks exceeding 2SD of the baseline and >10% the amplitude of the largest detected peak. These parameters allowed the initial detection of smaller and less typically shaped events and the post-hoc elimination of excessively small events that could be noise during a period of elevated baseline or a highly irregular peak possibly due to a PF burst.

As above, when comparing branches within a cell, we segregated deconvolved calcium events into the same five groups. The next step, determining if the events constituted a response to the stimulated whisker, was then performed on each subset of detected peaks individually.

As two 1min trials were conducted for each whisker, we concatenated the event amplitude and timing data from each trial of the same whisker. We then compared the event rise times (when the rising phase began) with the whisker stimulus times to assess how many peaks occurred during 150ms (5 frame) time windows after each whisker movement, as opposed to non-response windows of 150ms before each whisker movement or the 10s spontaneous time window when there was no whisker stimulation. Probabilities and amplitudes of response and non-response events were thus calculated for each ROI-averaged whole cell and individual

branch ROIs. Since whisker responses are known to be very sparse under anesthesia, we stimulated each whisker 100 times per trial (for a total of 200 trials over 2min) to experimentally bootstrap response probabilities. The repetition allowed us to calculate not only the absolute probability of response, but the variability of the response and non-response probabilities across frames relative to whisker movement time such that we could obtain a Z-score of the response probability using the following formula:

$$Z_{response} = \frac{Prob_{response} - Prob_{spontaneous}}{StDev_{spontaneous}}$$

For each set of input event times, if the $Z_{response} > 1.96$ (2SD) – high enough to reject H_0 with $\alpha < 0.05$ – then we considered this a response to the whisker.

Statistics and Quantifications

Statistical analysis was carried out using R (v4.2.1). Data following a normal distribution was tested with unpaired two-tailed Student's t-tests to compare two groups or ANOVA followed by a Tukey post-hoc correction for repeated measures to compare more than two groups and/or multiple factors. We used a one sample Student's t-test to compare individual groups with a specific, benchmark value where appropriate. Otherwise, for non-parameteric data, a Wilcoxon rank sum test was used for two group comparisons. We used a Pearson's Chi-squared test for independence to assess contingency tables from data with two non-continuous variables. Post-hoc comparisons of contingency tables from mouse and human cell count data were assessed with pairwise Z-tests of proportion with Bonferroni correction as the total numbers of cells differed greatly by species or sub-region, distorting the comparative strength of a standard chi-squared comparison of frequency. P-values and effect sizes (φ) of pairwise Z-tests are reported. To assess a relationship between two continuous variables, we used a linear regression and report the adjusted R^2 value and significance. For all analyses, $\alpha = 0.05$ was used to determine significance and figure panels refer to the significance of comparisons in the following way: ns $p > 0.05$, * $p \leq 0.05$, ** $p \leq 0.01$, *** $p \leq 0.001$.

Main Figures

Fig 1C: Pearson's Chi-squared, Ratio of cell morphologies ~ Lobule; n = 6,646 cells, $p < 0.001$, $\chi^2 = 170.18$.

Fig 1F: Pearson's Chi-squared, Ratio of cell morphologies ~ Lobule; n = 1,350 cells, $p < 0.001$, $\chi^2 = 106.83$.

Fig 1G: Morphology and Species: Pearson's Chi-squared, $p < 0.001$, $\chi^2 = 55.27$; Post-hoc pairwise Z-tests of proportion with Bonferonni correction: Normative, n = 598 and 268 cells, representing a mean ± SEM of 46.53 ± 2.2 and 5.82 ± 1.42 Percent of cells (%) in 30 and 20 lobules (mouse vs human); Split, n = 447 and 2977 cells in 30 and 21 lobules, 36.6 ± 2.04 and 47.7 ± 2.4 Percent of cells (%); Poly, n = 212 and 3401 cells in 29 and 21 lobules, 17.46 ± 2.45 and 46.76 ± 2.97 Percent of cells (%). All comparisons presented in table S3.

Fig 2D: Pearson's Chi-squared, Number of climbing fibers ~ Morphology; n = 159 cells, p = 0.003, $\chi^2 = 15.71$.

Fig 2E: 1 vs. 2+ CFs: n = 135 and 24 cells, -763.65 ± 2.51 and -978.75 ± 13.45 CF EPSC amplitude (pA), p = 0.006, Two-tailed Student's t-test; Weak CFs: n = 24 cells, -389.13 ± 10.3 CF EPSC amplitude (pA), p < 0.001, One-way Student's t-test, $\mu = 0$.

Fig 2F: 1 vs. 2+ CFs, all PCs: n = 135 and 24 cells, 43.74 ± 3.13 and 16.86 ± 3.28 Split distance (μm), p < 0.001, Two-tailed Student's t-test.

Fig 2G: 1 vs. 2+ CFs, mono-planar PCs: n = 85 and 9 cells, 54.48 ± 3.26 and 87.09 ± 7.73 Branch distance (μm), p = 0.002, Two-tailed Student's t-test.

Fig 2H: 1 vs. 2+ CFs, Poly PCs: n = 26 and 8 cells, 67.32 ± 5.7 and 95.91 ± 10 Trunk angle (°), p = 0.029, Two-tailed Student's t-test.

Fig 3F: Global vs. Local events: n = 95 cells, 0.29 ± 0.009 and 0.19 ± 0.007 Mean amplitude (ΔF/F0), p < 0.001, Two-tailed Student's t-test.

Fig 3G: Normative, Split, Poly: One-way ANOVA, p < 0.001; Tukey's HSD post-hoc, n = 32, 55, 8 cells, 17.36 ± 2.12, 36.62 ± 2.54, and 51.01 ± 9.76 Local events (%); Normative vs. Split, p < 0.001; Normative vs. Poly, p < 0.001; Split vs. Poly, p = 0.087.

Fig 3H: Normative, Split, Poly: Kruskal-Wallis test, p < 0.001; Pairwise Wilcoxon rank sum test, n = 32, 55, 8 cells, 0.37 ± 0.03, 0.24 ± 0.03, and 0.079 ± 0.04 Adjusted R^2; Normative vs. Split, p = 0.002; Normative vs. Poly, p < 0.001; Split vs. Poly, p = 0.016.

Fig 3I: Pearson's Chi-squared, Rate of significant branch covariation ~ Morphology; n = 95 cells, p = 0.007, $\chi^2 = 9.8$.

Fig 3J: Linear Regression, Inter-branch amplitude scale (sd) ~ Split distance (μm); n = 105 cells, p < 0.001, $R^2 = 0.099$.

Fig 3K: Linear Regression, excluding multi-planar cells, Inter-branch amplitude scale (sd) ~ Dendrite width (μm); n = 109 cells, p = 0.002, $R^2 = 0.078$.

Fig 4C: Normative, Split, Poly: One-way ANOVA, p < 0.001; Tukey's HSD post-hoc, n = 33, 112, 24 cells, 2.72 ± 0.36, 4.48 ± 0.29, and 5.78 ± 0.39 Mean local responses (#); Normative vs. Split, p = 0.004; Normative vs. Poly, p < 0.001; Split vs. Poly, p = 0.089.

Fig 4D: Normative, Split, Poly: One-way ANOVA, $p = 0.02$; Tukey's HSD post-hoc, n = 33, 112, 24 cells, 4.76 ± 0.42, 6.29 ± 0.33, and 6.96 ± 0.56 Inter-whisker difference (#); Normative vs. Split, $p = 0.041$; Normative vs. Poly, $p = 0.029$; Split vs. Poly, $p = 0.623$.

Fig 4F: Pearson's Chi-squared, Response category ~ Morphology; n = 169 cells, $p = 0.035$, $\chi^2 = 6.73$.

Fig 4G: Unresponsive, Global, and Lateral: One-way ANOVA, $p = 0.02$; Tukey's HSD post-hoc, n = 75, 42, 52 cells, 27.35 ± 2.06, 28.24 ± 3.58, and 18.73 ± 2.05 Split distance (μm); Unresponsive vs. Global, $p = 0.967$; Unresponsive vs. Lateral, $p = 0.034$; Global vs. Lateral, $p = 0.043$.

Fig 4H: Linear Regression, Local events (%) ~ Receptive field (whiskers); n = 151 cells, $p = 0.005$, $R^2 = 0.046$.

Fig 5C: Morphology and Stimulus Category: Two-way ANOVA, Morphology $p < 0.001$, Stimulus Category $p = 0.047$; Tukey's HSD post-hoc: Uni-modal, n = 24 and 38 cells, 18.06 ± 1.94 and 31.23 ± 2.98 Maximum local events (%), $Uni_{Normative}$ vs. $Uni_{Split+Poly}$, $p = 0.014$; Multi-modal, n = 24 and 38 cells, 21.11 ± 3.02 and 38.95 ± 3.01 Maximum local events (%), $Multi_{Normative}$ vs. $Multi_{Split+Poly}$, $p < 0.001$; $Uni_{Normative}$ vs. $Multi_{Normative}$, $p = 0.917$; $Uni_{Split+Poly}$ vs. $Multi_{Split+Poly}$, $p = 0.176$.

Fig 5F: Normative vs. Split+Poly PCs: n = 24 and 38 cells, 29.84 ± 3.51 and 45.58 ± 4.43 ΔBranch response range (%), $p = 0.008$, Two-tailed Student's t-test.

Fig 5G: Normative vs. Split+Poly PCs: n = 24 and 38 cells, -1.64 ± 1.44 and -1.57 ± 3.57 ΔBranch response mean (%), $p = 0.986$, Two-tailed Student's t-test.

Fig 5H: Normative vs. Split+Poly PCs: n = 24 and 38 cells, 31.47 ± 4.02 and 47.14 ± 5.55 ΔBranch response bilaterality (%), $p = 0.027$, Two-tailed Student's t-test.

Supplementary Figures

fig S3B: Pearson's Chi-squared, Morphology ~ Zebrin expression; n = 150 cells, $p = 0.078$, $\chi^2 = 5.09$. All comparisons presented in table S5.

fig S3E: Pearson's Chi-squared, Morphology ~ Zebrin expression; n = 162 cells, $p = 0.014$, $\chi^2 = 8.47$. All comparisons presented in table S6.

fig S4C: Pearson's Chi-squared, Morphology ~ Foliar sub-region.

Mouse: n = 1350 cells, p = 0.027, χ^2 = 10.96. All comparisons presented in table S7.

Human: n = 6645 cells, p < 0.001, χ^2 = 65.17. All comparisons presented in table S8.

figS4D: Pearson's Chi-squared, Dendrite orientation ~ Foliar sub-region.

Mouse: n = 1350 cells, p = 0.002, χ^2 = 17.41. All comparisons presented in table S9.

Human: n = 6645 cells, p < 0.001, χ^2 = 1876.9. All comparisons presented in table S10.

fig S5C: Pearson's Chi-squared, Multi-CF rate (%) ~ Split distance (µm); n = 159 cells, p = 0.025, χ^2 = 18.65.

fig S5D: 1 vs. 2+ CFs, non-Poly PCs excluding Normative PCs with no split: n = 79 and 16 cells, 36.77 ± 2.17 and 25.29 ± 3.25 Split distance (µm), p = 0.006, Two-tailed Student's t-test

fig S5E: 1 vs. 2+ CFs, non-Poly PCs: n = 79 and 16 cells, 96.97 ± 2.61 and 105.44 ± 4.95 Split angle (°), p = 0.16, Two-tailed Student's t-test.

fig S5F: 1 vs. 2+ CFs, Poly PCs: n = 26 and 8 cells, 67.32 ± 5.7 and 95.91 ± 10 Trunk angle (°), p = 0.029, Two-tailed Student's t-test.

fig S5G: 1 vs. 2+ CFs, all PCs excluding Normative PCs with no split: n = 104 and 24 cells, 66.85 ± 2.41 and 83.19 ± 6.05 Arbor separation (µm), p = 0.018, Two-tailed Student's t-test

fig S5H: 1 vs. 2+ CFs, Poly PCs: n = 26 and 8 cells, 21.23 ± 0.35 and 21.2 ± 0.49 Soma diameter (µm), p = 0.97, Two-tailed Student's t-test.

fig S5M: Linear Regression, CF EPSC amplitude (nA) ~ Age (days); n = 24 cells, p < 0.001, R^2 = 0.445.

fig S5N: Dominant CF to multi-CF PCs: Linear Regression, CF EPSC amplitude (nA) ~ Age (days); n = 24 cells, p = 0.235, R^2 = 0.021; Single CF to mono-CF PCs: Linear Regression, CF EPSC amplitude (nA) ~ Age (days); n = 126 cells, p = 0.383, R^2 = -0.002.

fig S5O: Normative, Split, and Poly: Kruskal-Wallis rank sum test, p = 0.21; Split vs. Poly PCs: n = 15 and 8 cells, 36.48 ± 1.23 and 53.96 ± 3.16 Small CF : big CF EPSC amplitude (%), p = 0.112, Two-tailed Student's t-test (p = 0.056, One-tailed Student's t-test).

fig S5P: Gyrus, Bank, and Sulcus: One-way ANOVA, p = 0.058; Tukey's HSD post-hoc, n = 6, 11, 7 cells, 27.91 ± 9.32, 40.69 ± 5.78, and 56.16 ± 7.04 Small CF : big CF EPSC amplitude (%); Gyrus vs. Bank, p = 0.431; Gyrus vs. Sulcus, p = 0.048; Bank vs. Sulcus, p = 0.27.

fig S5Q: Linear Regression, Small CF : big CF EPSC amplitude (%) ~ Trunk angle (°); n = 8 cells, p = 0.007, R^2 = 0.687.
fig S5R: Linear Regression, Small CF : big CF EPSC amplitude (%) ~ Split distance (μm); n = 23 cells, p = 0.138, R^2 = 0.059.

fig S6L: 1 vs. 2+ CFs, all PCs: n = 135 and 24 cells, 37.48 ± 0.79 and 42.58 ± 2.54 Age (days), p = 0.065, Two-tailed Student's t-test.

fig S7A: Normative, Split, Poly: One-way ANOVA, p = 0.028; Tukey's HSD post-hoc, n = 25, 29, 5 cells, 5.27 ± 1.18, 12.7 ± 2.58, and 16.74 ± 7.25 Local events (%); Normative vs. Split, p = 0.05; Normative vs. Poly, p = 0.11; Split vs. Poly, p = 0.75.
fig S7B: Normative, Split, Poly: One-way ANOVA, p = 0.01; Tukey's HSD post-hoc, n = 25, 29, 5 cells, 0.006 ± 0.07, 0.351 ± 0.08, and 0.19 ± 0.17 Ca^{2+} amplitude coefficient of variation between vs. within branches (CV); Normative vs. Split, p = 0.006; Normative vs. Poly, p = 0.71; Split vs. Poly, p = 0.77.
fig S7C: Linear Regression, Amplitude scale (sd) ~ Compartment separation (μm); n = 95 cells, p = 0.017, R^2 = 0.05.
fig S7D: Normative, Split, Poly: One-way ANOVA, p = 0.389; Tukey's HSD post-hoc, n = 32, 55, 8 cells, 1.26 ± 0.04, 1.38 ± 0.06, and 1.37 ± 0.17 Event rate (Hz); Normative vs. Split, p = 0.366; Normative vs. Poly, p = 0.757; Split vs. Poly, p = 0.998.
fig S7E: Split vs. Normative PCs: n = 13 animals, 102.72 ± 5.76 Split / Normative Rate (%), p = 0.645, One-way Student's t-test, μ = 100.
fig S7F: Linear Regression, Split / Normative Rate (%) ~ Local gap (%); n = 13 animals, p = 0.813, R^2 = -0.085.
fig S7G: Linear Regression, Rate above minimum (Hz) ~ Local events (%); n = 94 cells, p = 0.001, R^2 = 0.1.
fig S7H: Linear Regression, Event rate (Hz) ~ Local events (%); n = 95 cells, p = 0.008, R^2 = 0.06.
fig S7I: Normative, Split, Poly: One-way ANOVA, p = 0.043; Tukey's HSD post-hoc, n = 32, 55, 8 cells, 2.23± 0.09, 2.74 ± 0.14, and 2.71 ± 0.46 Event rate (Hz); Normative vs. Split, p = 0.036; Normative vs. Poly, p = 0.387; Split vs. Poly, p = 0.995.

fig S7J: Split vs. Normative PCs: n = 13 animals, 126.25 ± 8.29 Split / Normative Rate (%), p = 0.008, One-way Student's t-test, $\mu = 100$.
fig S7K: Linear Regression, Split / Normative Rate (%) ~ Local gap (%); n = 13 animals, p = 0.005, $R^2 = 0.48$.
fig S7L: Linear Regression, Rate above minimum (Hz) ~ Local events (%); n = 94 cells, $p < 0.001$, $R^2 = 0.14$.
fig S7M: Linear Regression, Event rate (Hz) ~ Local events (%); n = 95 cells, $p < 0.001$, $R^2 = 0.26$.
fig S7N: Normative, Split, Poly: One-way ANOVA, p = 0.019; Tukey's HSD post-hoc, n = 13, 16, 6 animals, 2.12 ± 0.23, 3.36 ± 0.47, and 2.85 ± 0.31 Event rate gap (Hz); Normative vs. Split, p = 0.014; Normative vs. Poly, p = 0.384; Split vs. Poly, p = 0.607.
fig S7O: Linear Regression, Event rate gap (Hz) ~ Local events (%); n = 95 cells, $p < 0.001$, $R^2 = 0.2$.
fig S7P: Minimum vs. non-minimum cells: n = 16 and 78 cells, 13.39 ± 4.93 and 22.21 ± 2.11 Local events (%), p = 0.032, Wilcoxon rank sum test.

fig S8E: Normative, Split, Poly: One-way ANOVA, p = 0.002; Tukey's HSD post-hoc, n = 28, 99, 22 cells, 22.32 ± 3.58, 36.88 ± 2.34, and 43.36 ± 4.29 Local events (%); Normative vs. Split, p = 0.007; Normative vs. Poly, p = 0.003; Split vs. Poly, p = 0.428.
fig S8F: Unresponsive, Global, and Lateral: One-way ANOVA, $p < 0.001$; Tukey's HSD post-hoc, n = 75, 42, 52 cells, 32.13 ± 2.62, 32.72 ± 3.24, and 46.76 ± 2.51 Local events (%); Unresponsive vs. Global, p = 0.988; Unresponsive vs. Lateral, $p < 0.001$; Global vs. Lateral, p = 0.004.

fig S9B: Pearson's Chi-squared, Response Type ~ Morphology; n = 2,520 and 3,990 events, 24 and 38 cells, $p < 0.001$, $\chi^2 = 169.13$.
fig S9C: Morphology and Stimulus Category: Two-way ANOVA, Morphology p = 0.88, Stimulus Category p = 0.002; Tukey's HSD post-hoc: Uni-modal, n = 24 and 38 cells, 70.37 ± 4.29 and 70.12 ± 4.03 Response probability (%), $Uni_{Normative}$ vs. $Uni_{Split+Poly}$, p = 0.999; Multi-modal, n = 24 and 38 cells, 82.22 ± 4.83 and 83.73 ± 3.53 Response probability (%),

$Multi_{Normative}$ vs. $Multi_{Split+Poly}$, $p = 0.994$; $Uni_{Normative}$ vs. $Multi_{Normative}$, $p = 0.285$; $Uni_{Split+Poly}$ vs. $Multi_{Split+Poly}$, $p = 0.053$.

fig S9D: Morphology and Stimulus Category: Two-way ANOVA, Morphology $p < 0.001$, Stimulus Category $p < 0.001$; Tukey's HSD post-hoc: Control, n = 24 and 38 cells, 5 ± 1.15 and 7.54 ± 1.38 Maximum local events (%), $Ctrl_{Normative}$ vs. $Ctrl_{Split+Poly}$, $p = 0.983$; Uni-modal, n = 24 and 38 cells, 18.06 ± 1.94 and 31.23 ± 2.98 Maximum local events (%), $Uni_{Normative}$ vs. $Uni_{Split+Poly}$, $p = 0.014$; Multi-modal, n = 24 and 38 cells, 21.11 ± 3.02 and 38.95 ± 3.01 Maximum local events (%), $Multi_{Normative}$ vs. $Multi_{Split+Poly}$, $p < 0.001$; $Ctrl_{Normative}$ vs. $Uni_{Normative}$, $p = 0.019$; $Ctrl_{Split+Poly}$ vs. $Uni_{Split+Poly}$, $p < 0.001$; $Uni_{Normative}$ vs. $Multi_{Normative}$, $p = 0.975$; $Uni_{Split+Poly}$ vs. $Multi_{Split+Poly}$, $p = 0.166$.

fig S9E: Morphology and Stimulus Category: Two-way ANOVA, Morphology $p < 0.001$, Stimulus Category $p < 0.001$; Tukey's HSD post-hoc: Control, n = 24 and 38 cells, 3.33 ± 0.8 and 4.74 ± 0.9 Directional maximum local events (%), $Ctrl_{Normative}$ vs. $Ctrl_{Split+Poly}$, $p = 0.997$; Uni-modal, n = 24 and 38 cells, 13.61 ± 1.73 and 23.33 ± 2.84 Directional maximum local events (%), $Uni_{Normative}$ vs. $Uni_{Split+Poly}$, $p = 0.029$; Multi-modal, n = 24 and 38 cells, 13.61 ± 1.77 and 26.14 ± 2.7 Directional maximum local events (%), $Multi_{Normative}$ vs. $Multi_{Split+Poly}$, $p = 0.001$; $Ctrl_{Normative}$ vs. $Uni_{Normative}$, $p = 0.043$; $Ctrl_{Split+Poly}$ vs. $Uni_{Split+Poly}$, $p < 0.001$; $Uni_{Normative}$ vs. $Multi_{Normative}$, $p = 1.0$; $Uni_{Split+Poly}$ vs. $Multi_{Split+Poly}$, $p = 0.914$.

fig S9F: Normative PCs: n = 24 cells, 3.06 ± 0.44 Uni vs. Multi-modal difference in maximum local events, $p = 0.171$, One-way Student's t-test, $\mu = 0$; Split+Poly PCs: n = 38 cells, 7.72 ± 0.34 Uni vs. Multi-modal difference in maximum local events, $p < 0.001$, One-way Student's t-test, $\mu = 0$.

fig S9I: Unimodal Normative vs. Split+Poly PCs: n = 24 and 38 cells, 21.41 ± 3.66 and 32.71 ± 4.41 ΔBranch response range (%), $p = 0.053$, Two-tailed Student's t-test; Multimodal Normative vs. Split+Poly PCs: n = 24 and 38 cells, 17.29 ± 2.14 and 27.44 ± 3.12 ΔBranch response range (%), $p = 0.01$, Two-tailed Student's t-test.

fig S9J: Unimodal Normative vs. Split+Poly PCs: n = 24 and 38 cells, -3.18 ± 2.11 and 3.73 ± 4.51 ΔBranch response mean (%), $p = 0.172$, Two-tailed Student's t-test; Multimodal Normative vs. Split+Poly PCs: n = 24 and 38 cells, -0.48 ± 1.43 and -4.11 ± 3.35 ΔBranch response mean (%), $p = 0.329$, Two-tailed Student's t-test.

fig S9K: Unimodal Normative vs. Split+Poly PCs: n = 24 and 38 cells, 24.59 ± 0.44 and 28.98 ± 6.63 ΔBranch response bilaterality (%), p = 0.602, Two-tailed Student's t-test; Multimodal Normative vs. Split+Poly PCs: n = 24 and 38 cells, 17.78 ± 2.52 and 31.56 ± 4.65 ΔBranch response bilaterality (%), p = 0.013, Two-tailed Student's t-test.

fig S10A: Pearson's Chi-squared, Morphology ~ Cells above threshold (%); n = 95 cells, p < 0.001, $\chi^2 = 19.33$.
fig S10B: Pearson's Chi-squared, Morphology ~ Cells above threshold (%); n = 169 cells, p = 0.03, $\chi^2 = 7.02$.
fig S10C: Pearson's Chi-squared without Yates' continuity correction, Morphology ~ Cells above threshold (%); n = 61 cells, p = 0.095, $\chi^2 = 2.78$.

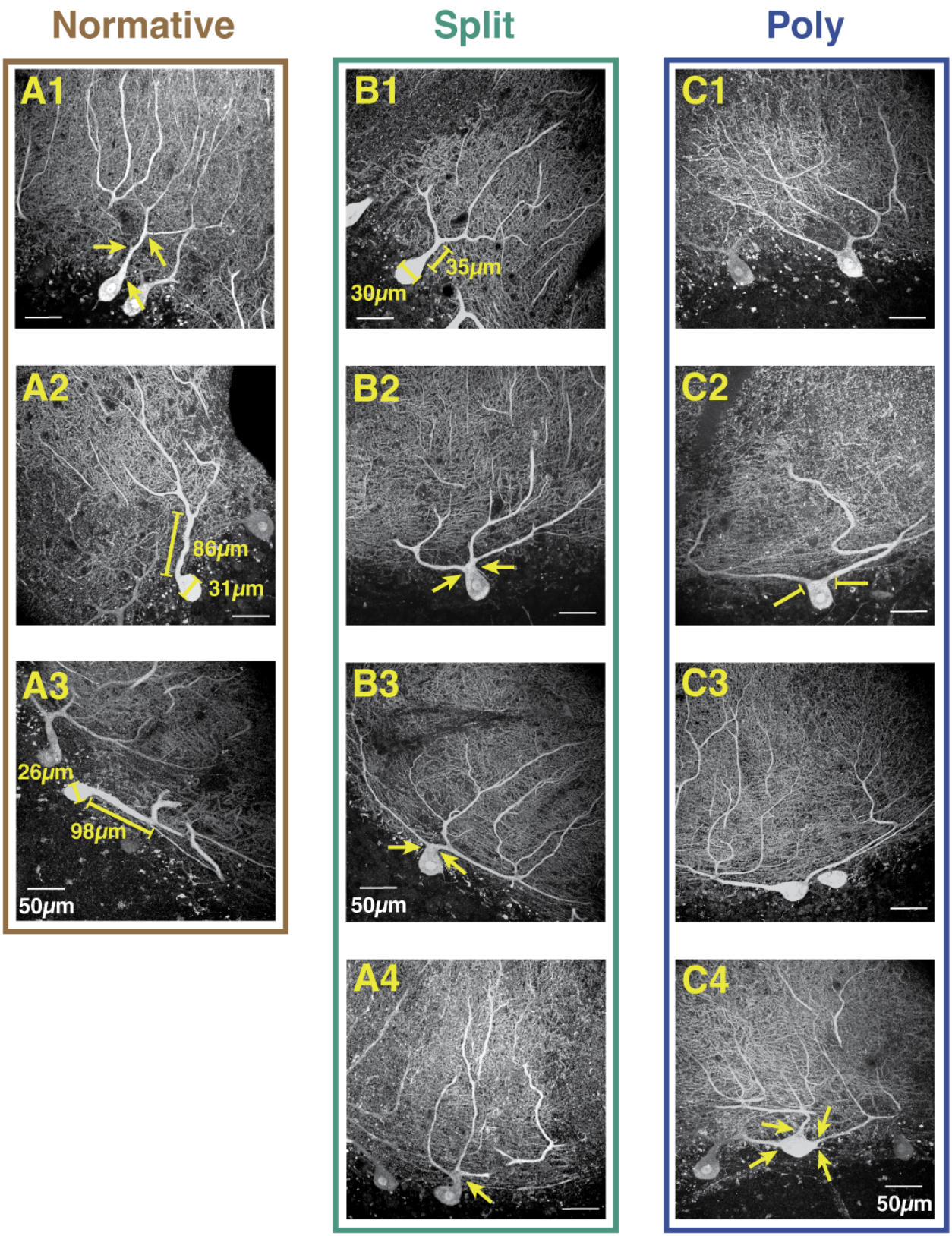
Normative
Split
Poly
A1
A2
86µm
31µm
A3
26µm
98µm
50µm
B1
35µm
30µm
B2
B3
50µm
A4
C1
C2
C3
C4
50µm

Fig. S1. Categorization of human Purkinje cells by proximal primary dendrite geometry
Human PCs were visualized in unembalmed tissue of one individual following immunolabeling for calbindin. (**A1-3**) Normative PCs have one trunk emerging from the soma and either 1) no bifurcation and no proximal minor branches ramifying >200μm laterally (**A1**) or 2) a bifurcation that is >2x the somatic diameter (**A2-3**). We used a threshold bifurcation distance of two somatic diameters measured from the base of the trunk where the circular dimension of the soma ends to the middle of the branch point. As seen in (**A2-3**), the visible bifurcations occur more than 2x the somatic diameter. To accelerate categorization, the distances were only measured when it was not obvious, as it was in most cases, whether the threshold was exceeded. (**B1-3**) Split PCs have one trunk emerging from the soma and either 1) no bifurcation but a large, proximal minor branch ramifying >200μm laterally or 2) a bifurcation that is <2x the somatic diameter (**B1**). Split PCs had spectrums of bifurcation distances and angles. (**B2-3**) The most challenging cases for categorization, which were common, presented with multiple primary dendrites emerging from a compartment which was difficult to define as somatic or dendritic. For our analyses we used the curvature of the space between the branch points and the center of the soma as an indication. As shown in (**B2-3**), there is a minor inward curvature of the superficial somatic compartment, like if the top of the soma was pinched into a single dendritic trunk from which the primary dendrite branches emerge. Compare this with (**C1-2**) where there is no pinching of the superficial soma such that the outer diameter merges directly with the primary dendrites and thus fits a definition of Poly PC. (**B4**) The most challenging cases for categorization, which were rare, presented with proximal bifurcations of the dendrite that were very proximal to the soma, but either asymmetrical or producing more than two primary dendrites. (**C1-4**) Poly PCs have multiple dendritic trunks emerging directly from the somatic compartment. Poly PCs had a spectrum of angles between emerging trunks, from acute (**C1**) or intermediate (**C2**) to emerging from opposite poles of a horizontally oriented somatic compartment. In the latter case, primary dendrites may continue ramifying in opposing directions to form entirely distinct and distant compartments as in (**C3**) or rapidly curve upward to preserve a somewhat compact set of compartments. (**C4**) While less common than two primary dendrites, we also observed many cases where Poly PCs had three or more dendrites emerging at varying relative angles.

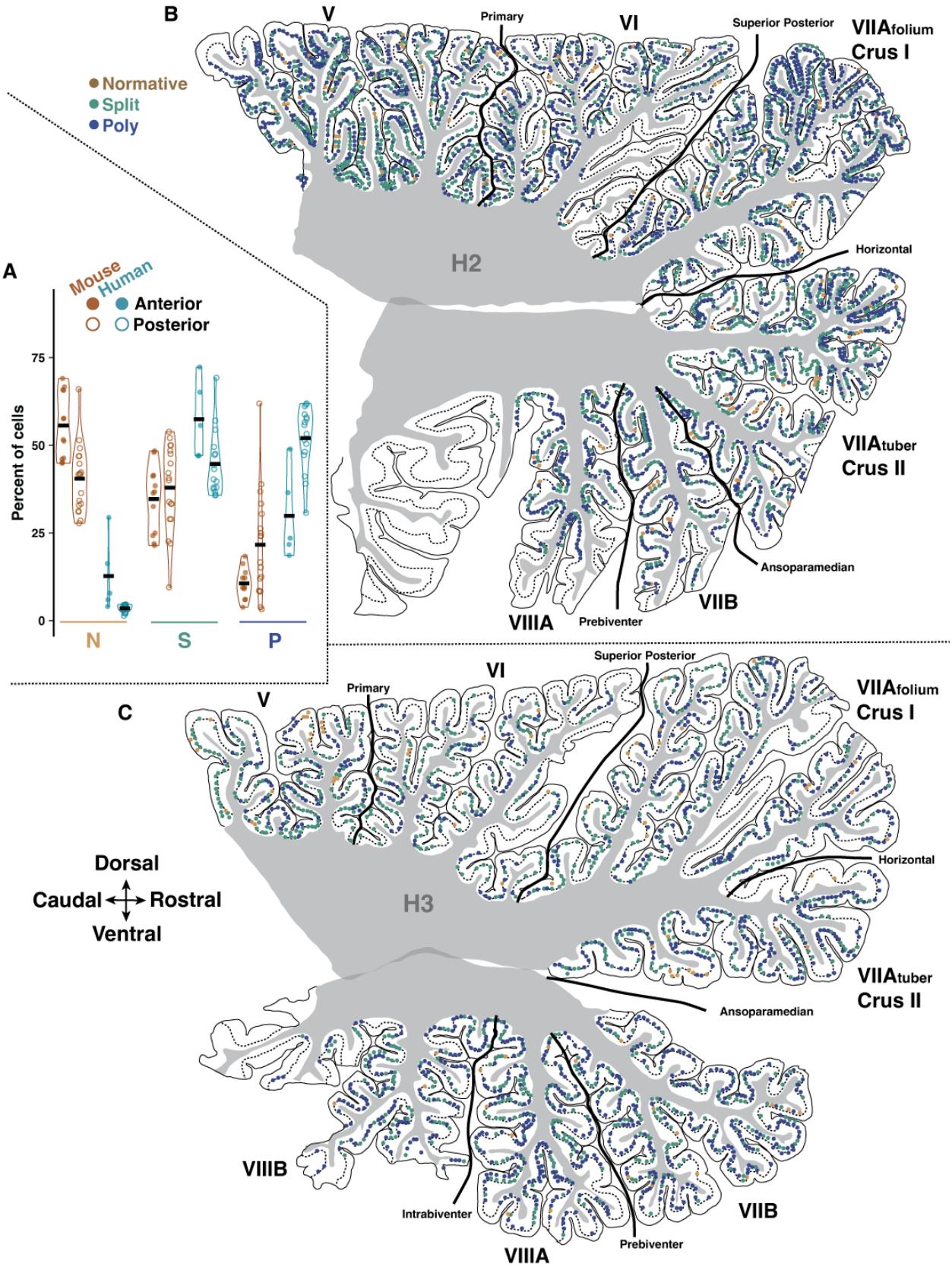
B
V
Primary
VI
Superior Posterior
VIIAfolium
Crus I
Normative
Split
Poly
H2
Horizontal
A
Mouse
Human
Anterior
Posterior
75
50
25
0
Percent of cells
N
S
P
VIIAtuber
Crus II
Ansoparamedian
VIIB
VIIIA
Prebiventer
C
Superior Posterior
VI
Primary
V
VIIAfolium
Crus I
Dorsal
Caudal
Rostral
Ventral
H3
Horizontal
VIIAtuber
Crus II
Ansoparamedian
VIIIB
Intrabiventer
VIIB
Prebiventer
VIIIA

Fig. S2. Reconstructed parasagittal sections of human cerebellar hemisphere
(**A**) Summary of relative cell morphology rates across anterior and posterior lobules of human and mouse (see table S4 for statistics). (**B-C**) Cross-section maps of human mid-hemisphere demonstrating the distribution of PC morphological types by region for individual specimens H2 and H3. H4 is presented in (Fig. 1B). See table S1 for quantification.

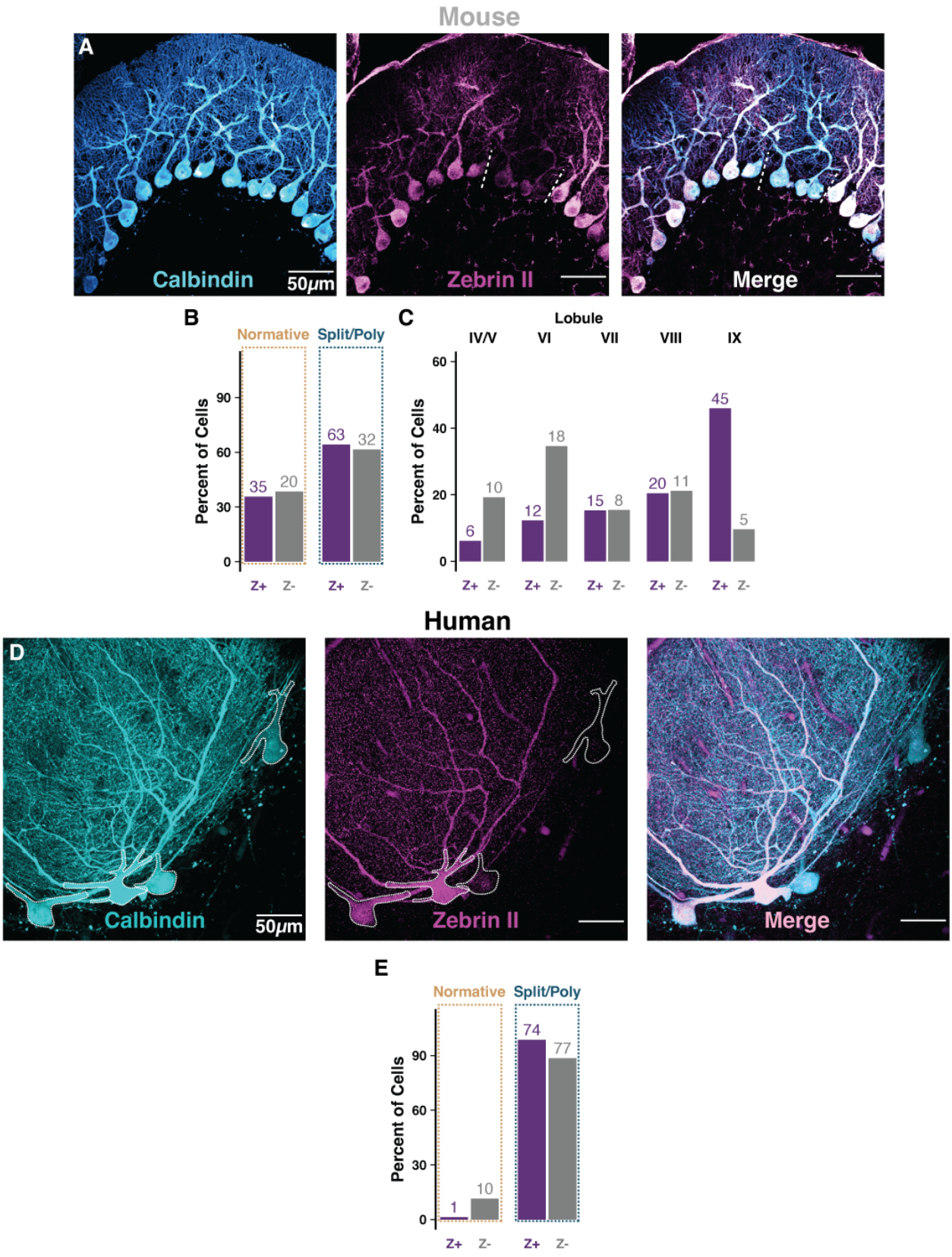
Mouse
A
Calbindin
50μm
Zebrin II
Merge
B
Normative
Split/Poly
Percent of Cells
0
30
60
90
35
20
63
32
Z+
Z-
C
Lobule
IV/V
VI
VII
VIII
IX
Percent of Cells
0
20
40
60
6
10
12
18
15
8
20
11
45
5
Human
D
Calbindin
50μm
Zebrin II
Merge
E
Normative
Split/Poly
Percent of Cells
0
30
60
90
1
10
74
77
Z+
Z-

Fig. S3. Zebrin expression does not predict Purkinje dendrite morphology in mouse or human. (**A**) Example maximum projection of parasagittally sliced mouse tissue dual labeled for calbindin (PCs) and aldolase-C (Zebrin II) shows a mixed population of normative and split cells at the borders of a zebrin- zone between zebrin+ zones. (**B**) Quantification of zebrin expression by morphological category shows no relationship (table S5, $\chi^2 = 0.024$ $p = 0.88$). (**C**) Quantification of zebrin expression by lobule shows the expected elevation of zebrin+ cells in posterior lobules. (**D**) Example maximum projection of parasagittally sliced human tissue dual labeled for calbindin (PCs) and aldolase-C (Zebrin II) shows two cells with distinct zebrin expression intensity despite similar calbindin labeling. (**E**) Quantification of zebrin expression by morphological category shows no relationship (table S6, $\chi^2 = 5.06$ $p = 0.024$) when PCs are classified as zebrin+ or zebrin- by their ratio of zebrin II to calbindin expression falling in the top or bottom 25^{th} percentiles.

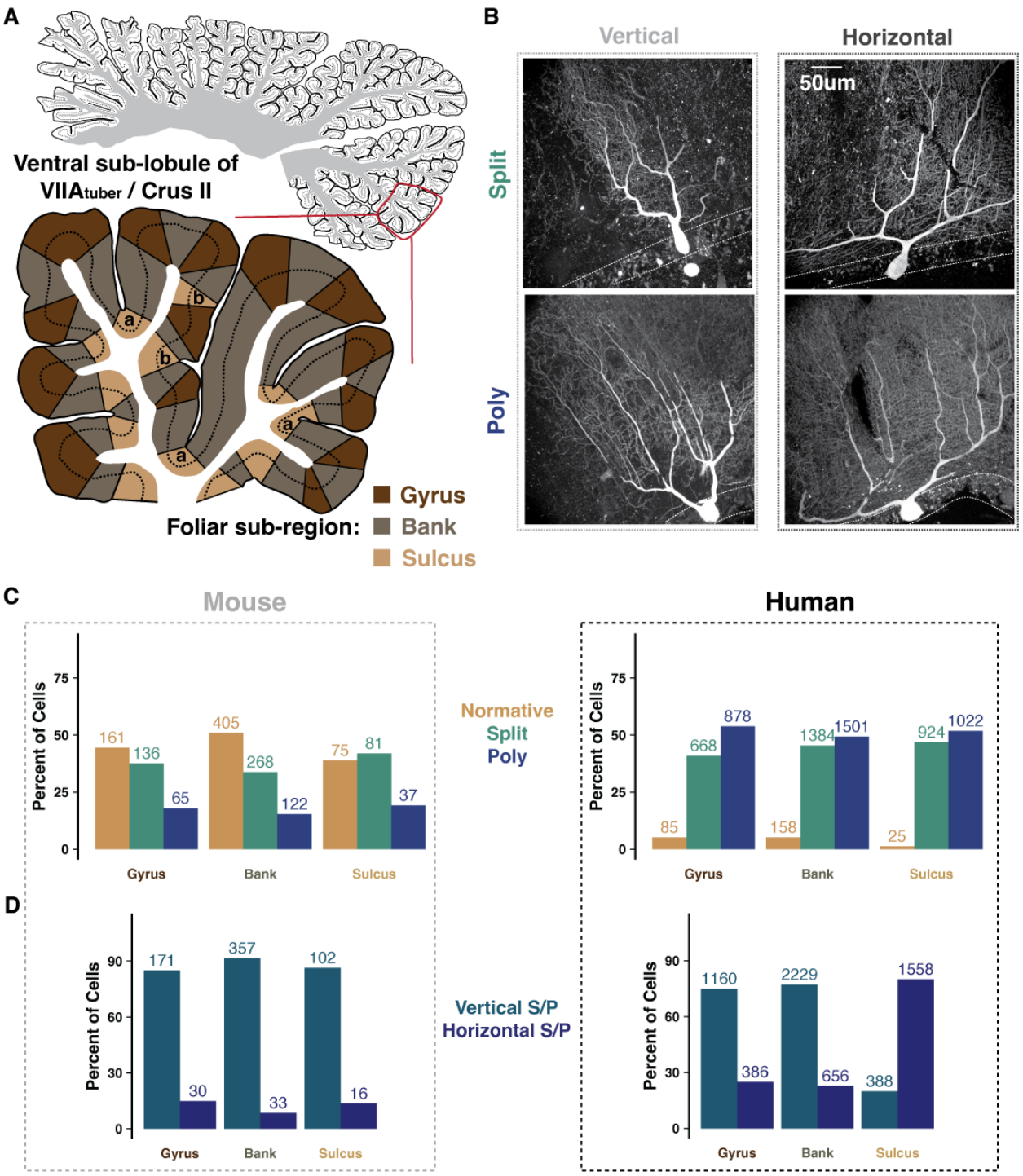
A
Ventral sub-lobule of
VIIAtuber / Crus II
a
b
b
a
a
Foliar sub-region:
Gyrus
Bank
Sulcus
B
Vertical
Horizontal
50um
Split
Poly
C
Mouse
Human
Percent of Cells
Normative
Split
Poly
161
136
65
405
268
122
75
81
37
85
668
878
158
1384
1501
25
924
1022
Gyrus
Bank
Sulcus
D
Vertical S/P
Horizontal S/P
171
30
357
33
102
16
1160
386
2229
656
388
1558

Fig. S4. Some features of Purkinje dendrite morphology correlate with foliar sub-region in human. (**A**) Schematic highlighting a ventral sub-lobule of $LVIIA_{tuber}$/Crus II from human specimen H4 and the definition of foliar sub-regions within that area. When marking PCs in the section, their location was denoted as Gyrus, Bank, or Sulcus (see materials and methods). Intermediate sulci embedded within a long bank region, indicated by "b", were combined with full sulci, indicated by "a". (**B**) Example human Purkinje cells belonging to each morphological category and with ramification patterns defined as either Vertical or Horizontal. (**C**) Quantification of the rate of each morphological category (Normative, Split, Poly) by foliar sub-region in mouse (left, table S7, $\chi^2 = 10.96$ $p = 0.027$) and human specimens (right, table S8, $\chi^2 = 65.17$ $p < 0.001$). While there were limited sub-regional variations in morphology in mice, many morphological features varied by sub-region in human. (**D**) As multi-innervated Split and Poly PCs in the mouse had wider separations in their dendritic arbor or a more obtuse angle between trunks emerging from the soma, we quantified the rate of vertical vs horizontal dendritic ramification (Vertical S/P and Horizontal S/P) in mouse (left, table S9, $\chi^2 = 17.41$ $p = 0.002$) and human specimens (right, table S10, $\chi^2 = 1876.9$ $p < 0.001$).

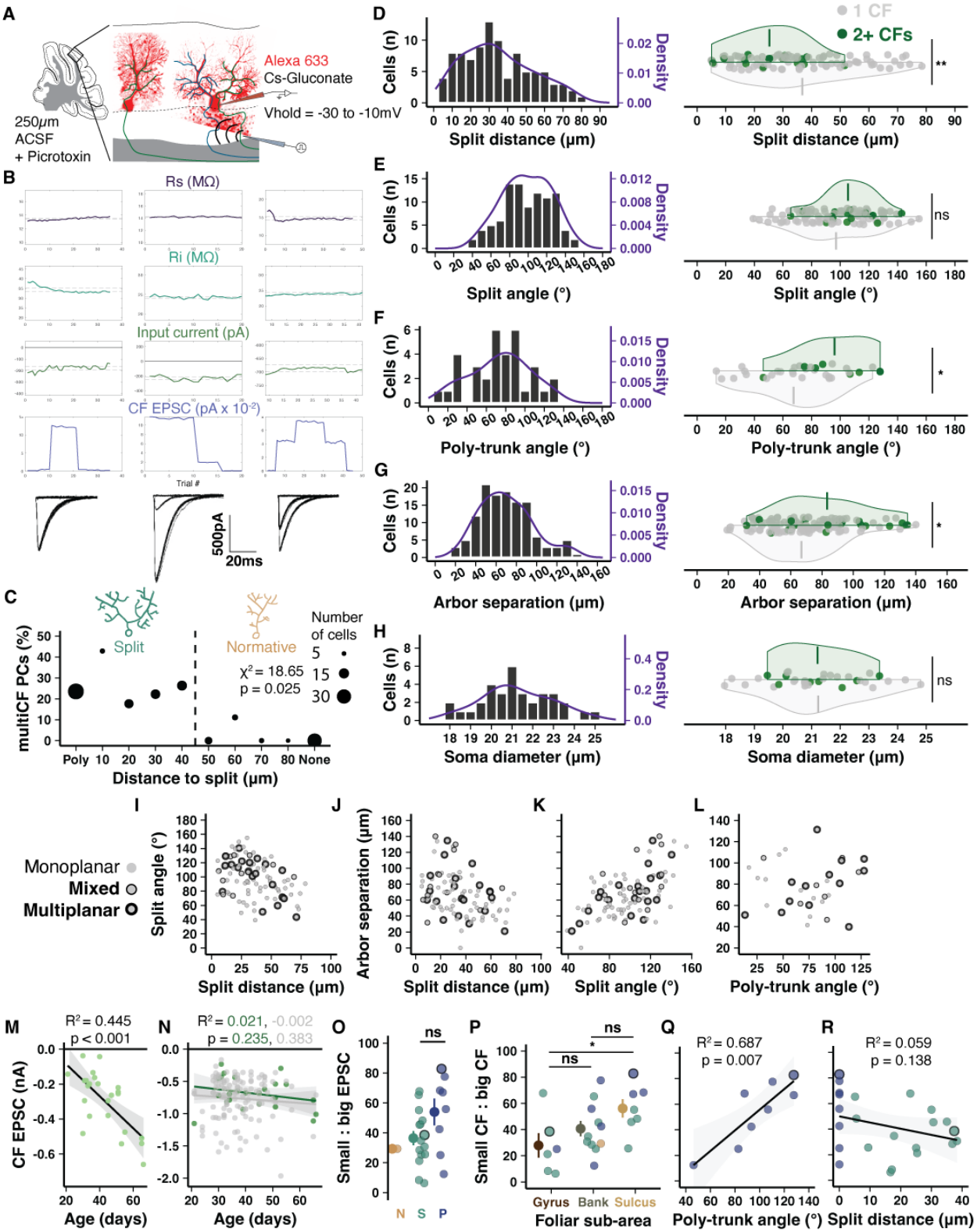
A
Alexa 633
Cs-Gluconate
Vhold = -30 to -10mV
250μm
ACSF
+ Picrotoxin
B
Rs (MΩ)
Ri (MΩ)
Input current (pA)
CF EPSC (pA x 10⁻²)
Trial #
500pA
20ms
C
Split
Normative
Number of cells
5
15
30
χ² = 18.65
p = 0.025
multiCF PCs (%)
Distance to split (μm)
D
Cells (n)
Density
Split distance (μm)
1 CF
2+ CFs
**
E
Split angle (°)
ns
F
Poly-trunk angle (°)
*
G
Arbor separation (μm)
*
H
Soma diameter (μm)
ns
I
Monoplanar
Mixed
Multiplanar
Split angle (°)
Split distance (μm)
J
Arbor separation (μm)
Split distance (μm)
K
Split angle (°)
L
Poly-trunk angle (°)
M
R² = 0.445
p < 0.001
CF EPSC (nA)
Age (days)
N
R² = 0.021, -0.002
p = 0.235, 0.383
Age (days)
O
Small : big EPSC
ns
N S P
P
Small CF : big CF
ns
*
ns
Gyrus Bank Sulcus
Foliar sub-area
Q
R² = 0.687
p = 0.007
Poly-trunk angle (°)
R
R² = 0.059
p = 0.138
Split distance (μm)

Fig. S5. Purkinje dendrite morphology correlates with climbing fiber multi-innervation. (**A**) Schematic of PC whole-cell patch-clamp recordings and CF stimulation in acute cerebellar slices. A cesium internal solution with Alexa 633 dye is used to reduce space clamp error, increase detection of more distant CF inputs, and label the cell for confocal imaging at the end of the experiment. Note, cesium and depolarized holding potentials distort the absolute size of the EPSC. (**B**) Representative physiology and CF-EPSC traces evoked by increasing and decreasing stimulation intensities. *Left*, a mono-innervated PC exhibits only one CF-EPSC amplitude regardless of stimulation intensity above threshold. *Middle*, a multi-innervated PC with discrete CF-EPSC amplitude steps constituting the stimulation of one small CF (~200pA) and then the summed EPSC amplitude of stimulating two CFs (~1.2nA) at a higher stimulation intensity. *Right*, discrete CF-EPSC steps indicating that this PC receives two CFs of approximately equal size (~400-450pA). (**C**) Inverse linear relationship between the rate of multi-innervation and distance from soma to primary dendrite split (n = 50 animals, 159 cells). (**D-H**) Whole population distributions (left) and distributions by CF innervation type (right) of morphological parameters: split distance (n = 79, 16), split angle (n = 79, 16), poly-trunk angle (n = 26, 8), arbor separation (n = 109, 16), and poly PC soma size (n = 26, 8). (**I-L**) Relationships between morphological parameters and Purkinje dendrite planarity. (**M**) Age dependency of weaker CF EPSC amplitude to multi-CF PCs indicates a possible continued development following circuit maturation (n = 24). (**N**) In contrast, neither the dominant CF on multi-CF PCs (green, n = 24) nor lone CFs of mono-innervated PCs (grey, n = 135) show a relationship between age and EPSC amplitude. (**O**) The ratio of EPSC amplitudes between strong and weak CF inputs to multi-innervated PCs are widely varied across cell morphologies. Bordered points indicate cells with 3 CFs where the smallest of the three inputs is compared with the largest (n = 24 cells). (**P**) Among all multi-innervated PCs, the ratio of EPSC amplitude between the smaller and larger detected CF is smaller in the gyrus (28%) than the sulcus (56%; n = 6, 11, 7 cells), which builds on the finding that multi-innervation is enhanced in sulcus of the vermis (29). (**Q**) Among multi-innervated Poly PCs, a wider dendrite separation angle correlates with greater EPSC amplitude parity between multiple CFs (n = 8 cells). (**R**) Among multi-innervated PCs, an earlier dendrite split (0 for Poly PCs) does not correlate with greater EPSC amplitude parity (n = 23).

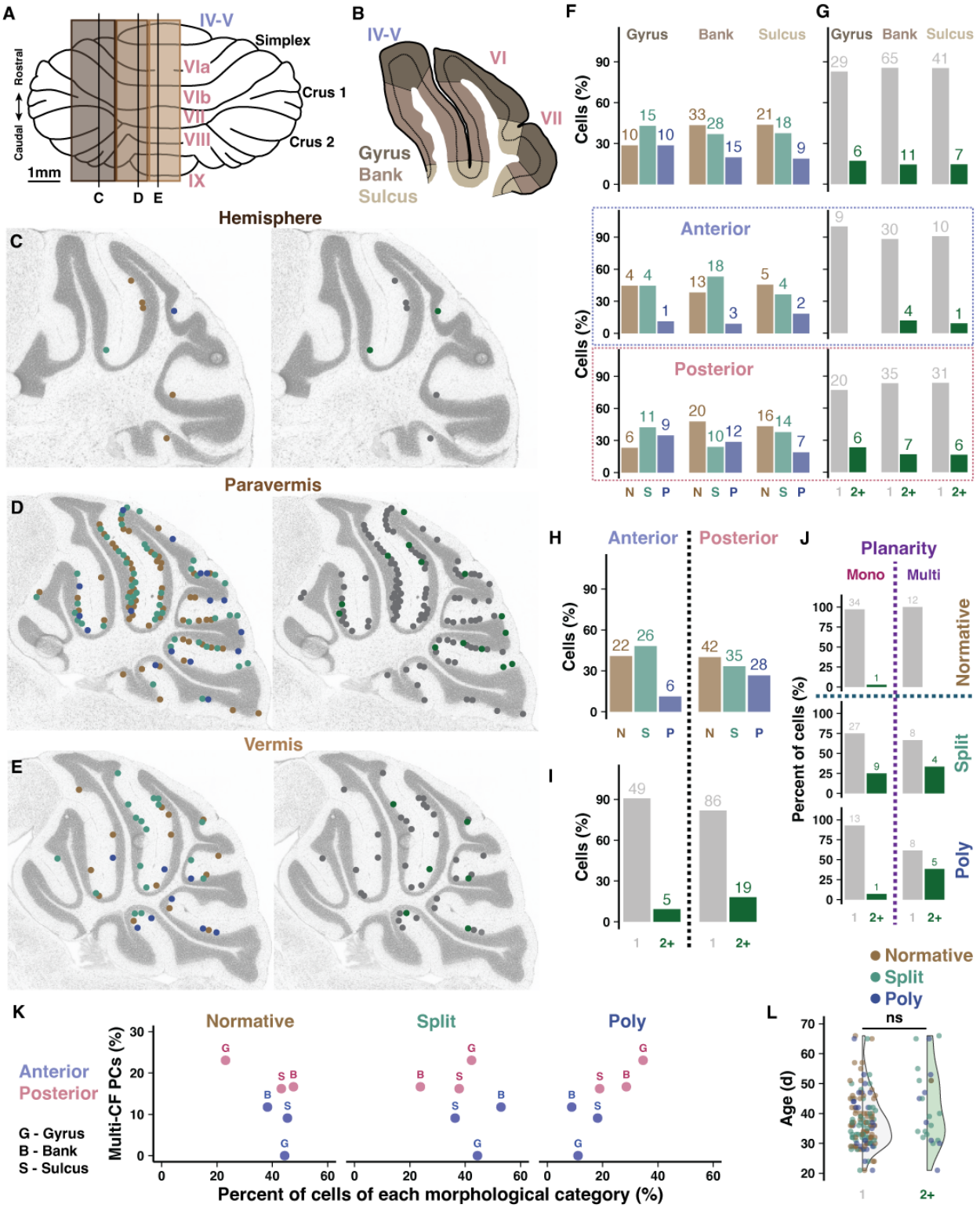
A
IV-V
Simplex
VIa
VIb
VII
VIII
IX
Crus 1
Crus 2
Rostral
Caudal
1mm
C
D
E
B
IV-V
VI
VII
Gyrus
Bank
Sulcus
Hemisphere
C
Paravermis
D
Vermis
E
F
Gyrus
Bank
Sulcus
Cells (%)
Anterior
Posterior
N S P N S P N S P
G
Gyrus Bank Sulcus
1 2+ 1 2+ 1 2+
H
Anterior
Posterior
Cells (%)
N S P N S P
I
Cells (%)
1 2+ 1 2+
J
Planarity
Mono
Multi
Normative
Split
Poly
Percent of cells (%)
K
Normative
Split
Poly
Anterior
Posterior
G - Gyrus
B - Bank
S - Sulcus
Multi-CF PCs (%)
Percent of cells of each morphological category (%)
L
Normative
Split
Poly
ns
Age (d)
1
2+

Fig. S6. Prevalence of climbing fiber multi-innervation and dendritic morphology across cerebellar regions. (**A**) Schematic of the mouse cerebellum and the medio-lateral location of acute slices used in whole cell patch clamp recordings. (**B**) Example of a sagittal section demonstrating the division of foliar sub-areas. (**C-E**) Slice maps indicating the location of each recorded PC and its morphology (left) or CF innervation pattern (right, multi-CF PCs are green). (**F-G**) Distribution of morphological type (left) or CF innervation pattern (right) across foliar sub-areas for all cells (top) or by lobule region (bottom, anterior vs posterior). Numbers above bars are absolute number of cells. (**H-I**) Distribution of morphological type (**H**) or CF innervation pattern (**I**) by lobule region without sub-dividing foliar sub-area. (**J**) Ratios of multi-innervated PCs by morphology or dendritic planarity. Dendrite planarity has been linked to CF innervation patterns previously (*65*), but we find that the presence of multiple primary dendrites – largely requisite to multiplanarity – is slightly more predictive of CF multi-innervation (4 : 96% vs. 55 : 45%). Some PCs could not be clearly identified by planarity, so only a subset of data is presented. (**K**) Relationship between percent of cells with multi-CF innervation across lobule region (anterior in blue, posterior in pink) and foliar sub-area (G – gyrus, B – bank, S – sulcus) and the percent of cells of either Normative, Split, or Poly structure. (**L**) No effect of age on the presence of CF multi-innervation (n = 135 and 24 cells).

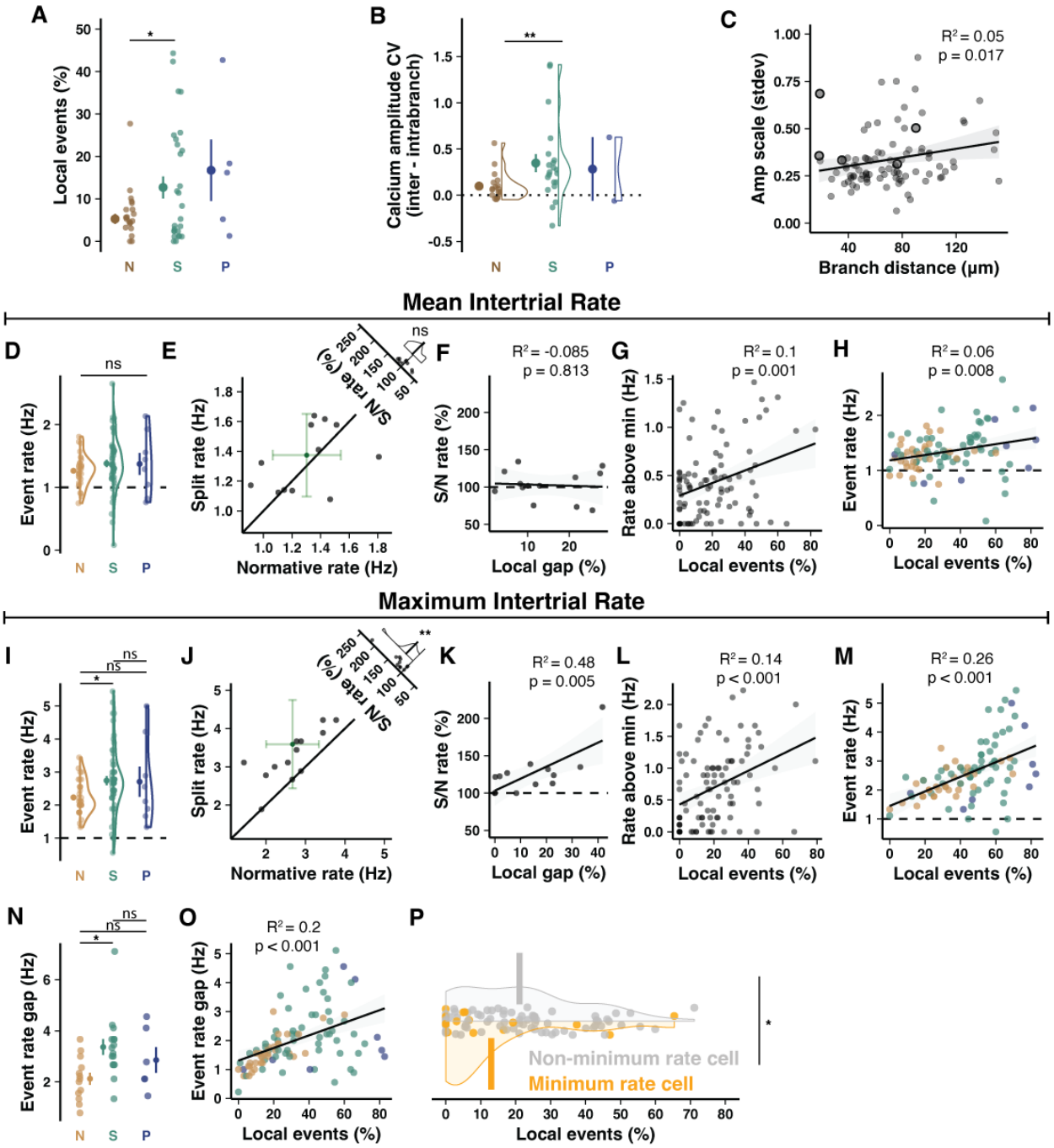
A
Local events (%)
N
S
P
B
Calcium amplitude CV (inter - intrabranch)
C
Amp scale (stdev)
R² = 0.05
p = 0.017
Branch distance (μm)
Mean Intertrial Rate
D
Event rate (Hz)
ns
E
Split rate (Hz)
Normative rate (Hz)
S/N rate (%)
F
R² = -0.085
p = 0.813
Local gap (%)
G
R² = 0.1
p = 0.001
Rate above min (Hz)
Local events (%)
H
R² = 0.06
p = 0.008
Event rate (Hz)
Local events (%)
Maximum Intertrial Rate
I
J
K
R² = 0.48
p = 0.005
L
R² = 0.14
p < 0.001
M
R² = 0.26
p < 0.001
N
Event rate gap (Hz)
O
R² = 0.2
p < 0.001
P
Non-minimum rate cell
Minimum rate cell
Local events (%)

Fig. S7. Characterizing calcium signal heterogeneity and subsequent elevation of event rate and total dynamic range. (**A**) Local events identified manually in a subset of data finds a lower baseline frequency of local events but an identical pattern of elevation in Split and Poly PCs (n = 16 animals, n = 25, 29, and 5 cells). (**B**) Analyzing the coefficient of variation of event amplitudes within vs. between branches of each cell shows that, compared to Normative cells, Split PCs have more variability between branches that is not found within branches. This indicates that heterogeneity is a feature of dendritic macro-compartments instead of small sub-branches within a primary dendrite (n = 16 animals, n = 25, 29, and 5 cells). (**C**) Variability of the inter-event amplitude scale (the mean ratio of event amplitude between branches) as a function of the distance between the centroid of dendritic branches (n = 23 animals, n = 95 cells). (**D-H**) Converging CFs likely originate from neighboring IO cells with local synchrony via gap junction coupling and convergence of IO input pathways. Thus, multiple converging CFs likely exhibit some overlapping activity and supply only modest elevations of input frequency. To test this, we compared total CF-dependent event rates to the quantity of heterogeneity. Lateral crus I PCs are largely zebrin(+), but may still have modest variation in zebrin identity and therefore CF input rate (*66*). To compensate, we analyzed raw and normalized inter-trial event rates pooled across PCs and animals. When mean spontaneous event rate is measured during control trials, we made several observations. (**D**) There is no difference between mean event rates by morphology (n = 23 animals, n = 32, 55, and 8 cells). (**E**) To control for differences in CF input rates based on PC molecular patterning identities, we can analyze only cells in animals where Split and Normative cells were both present in a local field of view. There is no bias in the Split relative to Normative PC mean rate within each animal (n = 13 animals). (**F**) Relatedly, there is no relationship between the local event ratio difference between Normative and Split PCs (Local ratio gap) and the ratio of Split to Normative PC event rates (n = 13 animals). (**G**) Controlling for event rate differences across animals by normalizing event rates to the local minimum shows an elevation of event rates, regardless of morphology, in PCs with higher local event ratios (n = 23 animals, n = 94 cells). (**H**) As in J, but without normalizing event rate, PCs with higher local event ratios have modestly elevated event rates (n = 23 animals, n = 95 cells). (**I-M**) Numerous variables could be minimizing the effect size observed by using the mean event rate. On the other hand, analyzing the maximum event rate might provide a more direct indication of the elevation of event rate afforded by putative multi-CF innervation. Thus, we performed the same measurements as in (**D-H**) but using the *maximum* rate of spontaneous events during the same control trials. (**I**) A significant difference emerges in event rates by morphology (n = 23 animals, n = 32, 55, and 8 cells). (**J**) Across animals, Split PCs have higher maximum event rates than Normative PCs (n = 13 animals). (**K**) Animals with a larger difference between local event ratios of split PCs relative to Normative PCs also show a higher event rate in Split PCs (n = 13 animals). (**L**) The maximum rate above the minimum local cell rate is higher in PCs with more local events (n = 23 animals, n = 94 cells). (**M**) PCs with higher local event ratios, particularly Split and Poly, also have elevated event rates (n = 23 animals, n = 95 cells). (**N**) The difference in result between using mean and maximum event rate is partly explained by the fact that Split PCs have wider variability in event rates, with mostly higher maximums and slightly lower minimums, suggesting a larger dynamic range of activity. This is confirmed by computing the gap between minimum and maximum spontaneous event rates during control trials for each cell and comparing Split and Normative PCs (n = 17 animals, n = 13, 16, 6). (**O**) The event rate gap also correlates with the local event ratio (n = 23 animals, n = 95 cells). (**P**) PCs with the

minimum spontaneous event rate in each animal (orange) have lower local event rates than the remaining cells (grey, n = 17 animals, n = 17 and 77 cells).

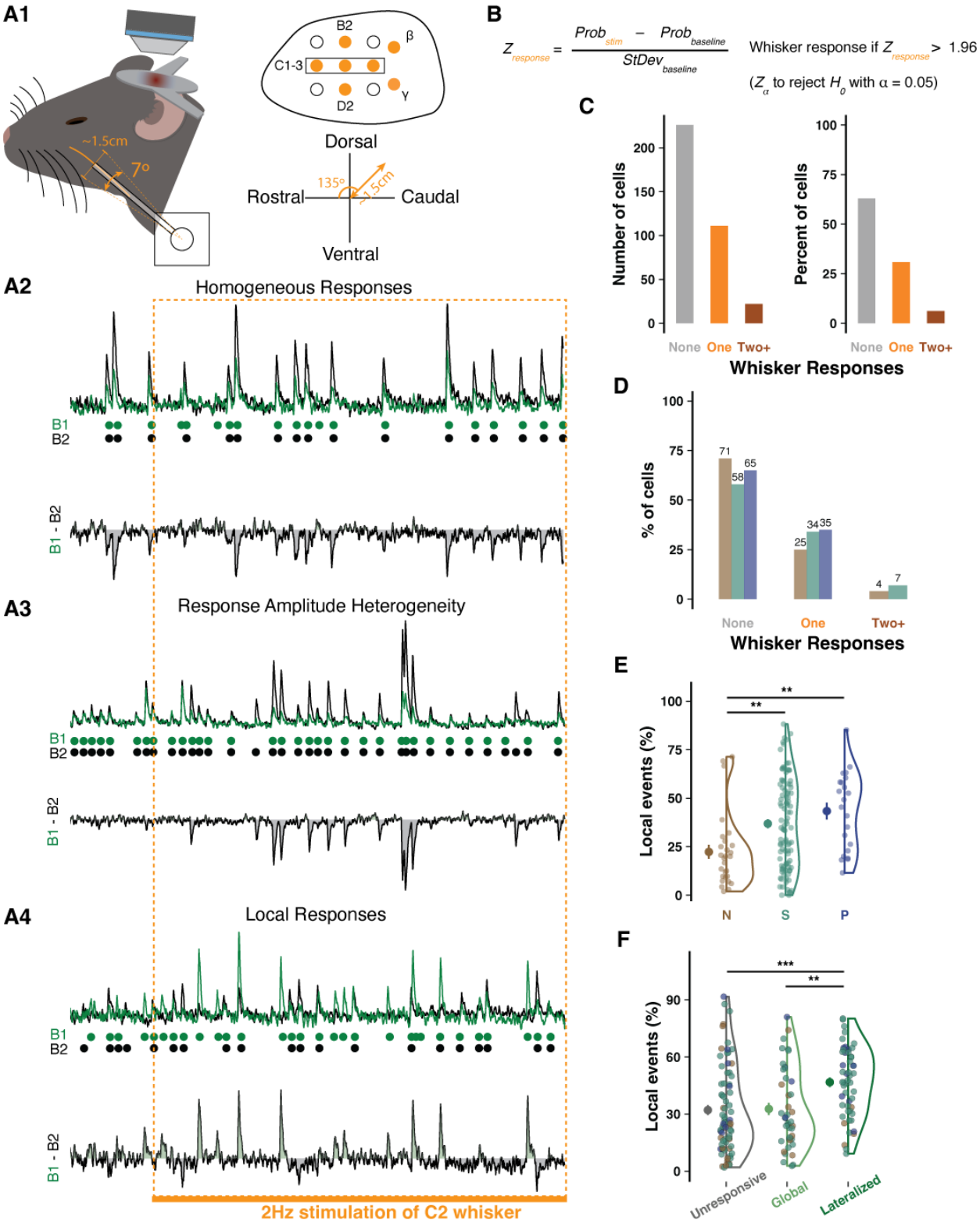
A1
~1.5cm
7°
B2
β
C1-3
γ
D2
Dorsal
Rostral
Caudal
Ventral
135°
1.5cm
B
$Z_{response} = \frac{Prob_{stim} - Prob_{baseline}}{StDev_{baseline}}$
Whisker response if $Z_{response} > 1.96$
(Z_α to reject H_0 with $\alpha = 0.05$)
C
Number of cells
Percent of cells
None One Two+
Whisker Responses
D
% of cells
71
65
58
25
34
35
4
7
None One Two+
Whisker Responses
A2
Homogeneous Responses
B1
B2
B1 - B2
A3
Response Amplitude Heterogeneity
B1
B2
B1 - B2
A4
Local Responses
B1
B2
B1 - B2
2Hz stimulation of C2 whisker
E
Local events (%)
**
**
N
S
P
F
Local events (%)
***
**
Unresponsive
Global
Lateralized

Fig. S8. Purkinje cell responses to single whisker stimulation match the literature and branch-specific events match other recording methods. (A) Schematic of rotary servo motor stimulation of individual whiskers. Whiskers B2, D2, C1-3, β, and γ were stimulated one at a time for two trials each in a random order in each mouse. The servo motor was programmed via an Arduino synchronized to the imaging time to rotate 7° at 2Hz and was positioned to move each whisker in the dorso-caudal direction (135°). (**A2**) Sample traces from a PC with homogeneous activity and responses during the same trial of stimulation of the C2 whisker as shown in different PCs with either largely global responses but dynamic amplitude scaling (**A3**) or with many local responses in addition to dynamic global response amplitude scaling (**A4**). (**B**) The formula used to determine if events in an ROI constitute a response. A z-scored probability of response is obtained by finding the difference between the probability of an event during baseline vs. response time windows and dividing by the deviation of the probability during baseline periods. If the Z-score exceeded two standard deviations, $Z_{response} > 1.96$, we could reject H_0 that there was no response with a confidence of $\alpha = 0.05$). (**C**) Relative rates of non-response (60%) and response to one (25%) or more whiskers (15%) for cells using combined (averaged) branch signal, the typical approach in the field, as opposed to total responses extracted separately from each branch. These values match the expected rate described by Ju and colleagues (46). (**D**) The relative rates as in (**C**) separated by cell morphology. A slight elevation in response rate can be observed in Split and Poly PCs, even when only assessing the averaged dendritic signal. As shown in Fig. 4D, deconvolving events and responses separately for each primary dendrite in the same cell population produced a higher fidelity representation of whisker responses, which revealed more responsiveness than detected with averaged dendritic signal. Crucially, this elevation of detected responsiveness was especially pronounced in Split and Poly PCs, while Normative PC response rates were largely unchanged. (**E**) Rates of spontaneous, branch-specific events by morphological category during recordings in medial Crus I while mice were under anesthesia (n= 13 animals, n = 28, 99, 22 cells). These rates are nearly identical to rates in awake conditions recorded from lateral Crus I. (**F**) PCs with lateralized responses have more branch-specific events (45%) than PCs with global or no response (both 25%, n = 75, 42, 52 cells).

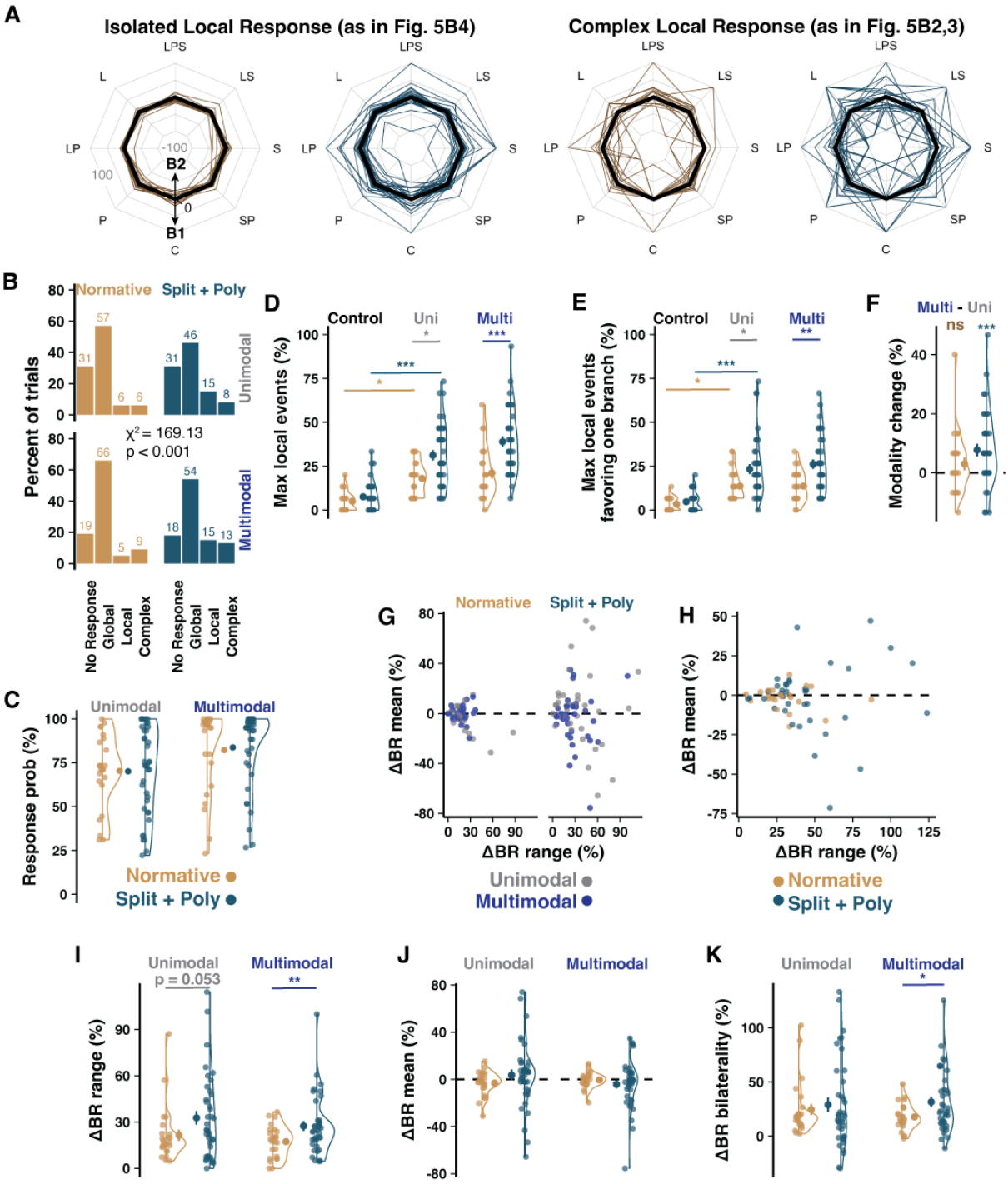
A
Isolated Local Response (as in Fig. 5B4)
Complex Local Response (as in Fig. 5B2,3)
LPS
LS
S
SP
C
P
LP
L
-100
100
B2
B1
0
B
Normative
Split + Poly
Unimodal
Multimodal
Percent of trials
χ² = 169.13
p < 0.001
No Response
Global
Local
Complex
C
Response prob (%)
Normative
Split + Poly
D
Control
Uni
Multi
Max local events (%)
E
Max local events favoring one branch (%)
F
Multi - Uni
ns
Modality change (%)
G
ΔBR mean (%)
ΔBR range (%)
H
I
Unimodal
Multimodal
p = 0.053
ΔBR range (%)
J
ΔBR mean (%)
K
ΔBR bilaterality (%)

Fig. S9. Multisensory CF receptive field representation across Purkinje cell branches. (**A**) Radar plots of non-absolute (directional) local event rates (in isolation, *top*, or as part of a response with global and local components, *bottom*) favoring arbitrarily designated branch 1 or branch 2 of each PC. Middle back line marks no local responses whereas lines deviating toward the outside or inside of the radar indicate high ratios of local events favoring one or the other branch. (**B**) Ratios of uni- and multisensory response type by morphology (n = 2,520 and 3,990 events, from 24 and 38 cells). (**C**) Average response probability (here and below: n = 12 animals, n = 24 Normative and 38 Split+Poly cells). (**D**) As in (Fig. 5C), the highest percentage of local events regardless of branch identity, across stimuli for each cell. (**E**) Obtaining the difference between the number of local responses from each branch for each stimulus – if both branches have local responses to a stimulus this determines how many more local responses one branch had over the other – gives the directionality of the local responses as favoring one branch or the other. Taking the maximum absolute value gives the maximum directional rate. (**F**) Relative difference of maximum local events between uni- and multisensory stimuli reveals no change in Normative PCs but a modest increase of local events in SP PCs during multisensory stimulation. (**G-H**) The relationship between range and directional ΔBR mean grouped by sensory modality category (uni vs. multi-sensory) or morphology (Normative vs. Split+Poly). (**I-J**) As in (Fig. 5F-G), the ΔBranch Response (ΔBR) range and mean, but here separated by uni- vs multisensory stimulus types instead of combined (Student's t-test). (**K**) As in (Fig. 5H), subtracting the ΔBR mean from the range distinguishes cells with either unilateral or bilateral profile of modality representations. Unilateral cells (high ΔBR range and mean) have one branch that shows branch-specific responses to some but not all modalities, whereas both branches of bilateral cells (high ΔBR range and low ΔBR mean) show branch-specific responses to different modalities.

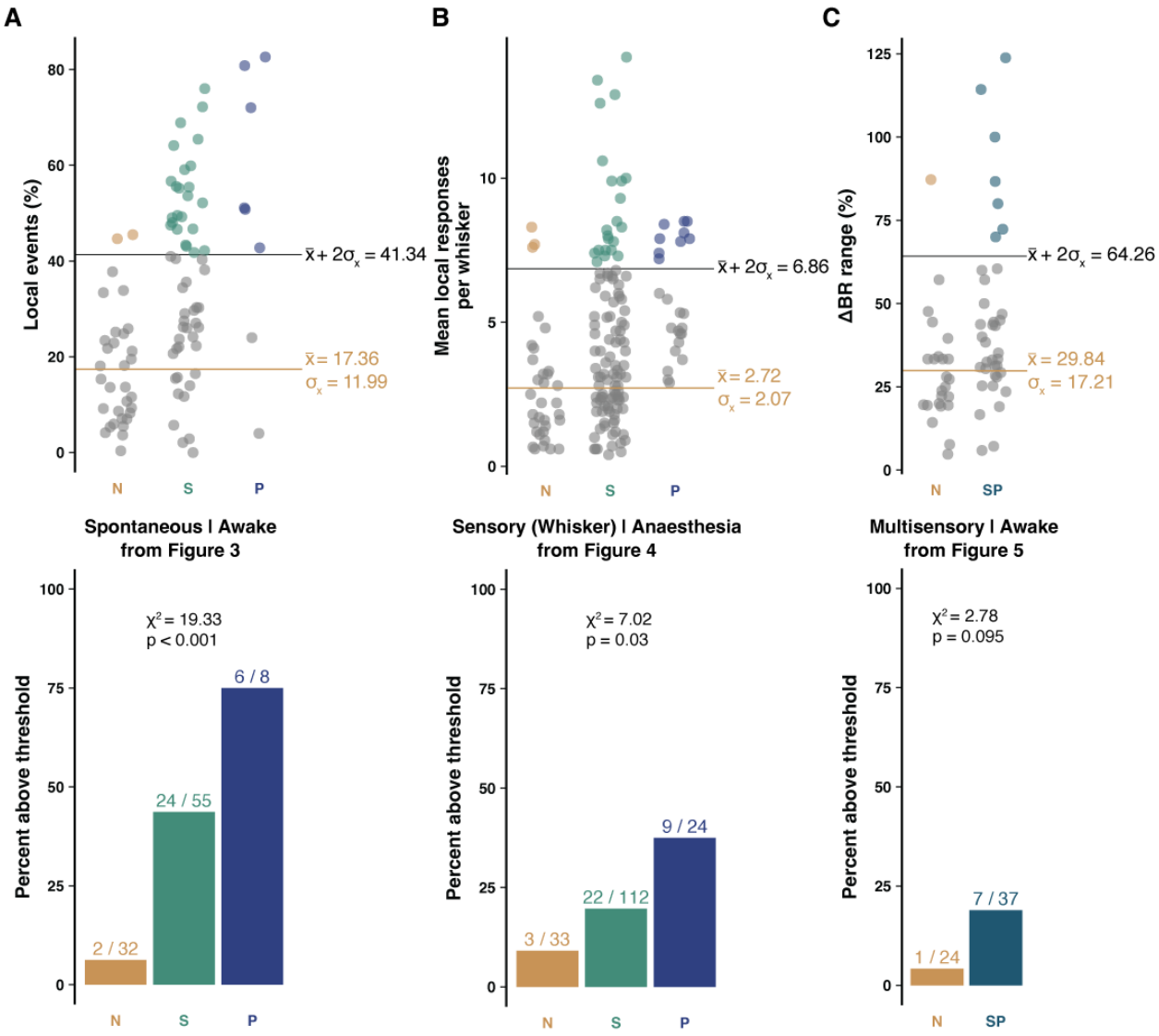
A
Local events (%)
x̄ + 2σx = 41.34
x̄ = 17.36
σx = 11.99
N
S
P
Spontaneous | Awake
from Figure 3
Percent above threshold
χ² = 19.33
p < 0.001
2 / 32
24 / 55
6 / 8
B
Mean local responses per whisker
x̄ + 2σx = 6.86
x̄ = 2.72
σx = 2.07
Sensory (Whisker) | Anaesthesia
from Figure 4
χ² = 7.02
p = 0.03
3 / 33
22 / 112
9 / 24
C
ΔBR range (%)
x̄ + 2σx = 64.26
x̄ = 29.84
σx = 17.21
SP
Multisensory | Awake
from Figure 5
χ² = 2.78
p = 0.095
1 / 24
7 / 37

Fig. S10. Comparative statistics across Ca^{2+} imaging datasets shows similar absolute and relative rates of enhanced heterogeneity in Split and Poly PCs as of multi-innervation in slice electrophysiology. To obtain an approximate quantification of potential CF multi-innervation from the two-photon imaging data that can be compared to the quantification obtained from the *in vitro* patch-clamp recordings, we extracted percentages of local events from our datasets, comparing Split and Poly PCs to Normative PCs. We obtained the mean ($\bar{x}$) and standard deviation (σ_x) of the Normative population and defined the threshold as values exceeding $\bar{x} + 2\,\sigma_x$ (e.g. Z-score of 2). We then applied this threshold across different measures of heterogeneity from different datasets. (**A**) Applying the threshold to local event rate data (top) under spontaneous conditions where the mice were awake and resting (data from Fig. 3G), we observe enhanced heterogeneity in 6%, 43%, and 75% of Normative, Split, and Poly PCs, respectively (bottom). See also the ratios of PCs without significant correlations between branch activity in Fig. 3I. (**B**) Applying the threshold to the number of evoked local whisker responses while the mice were under ketamine anesthesia (data from Fig. 4C), we observe enhanced heterogeneity in 9%, 20%, and 38% of Normative, Split, and Poly PCs, respectively. (**C**) Applying the threshold to the range of the Δbranch response profiles across multi-sensory stimuli while the mice were awake (data from Fig. 5F), we observe enhanced heterogeneity in 4% and 19% of Normative and Split/Poly PCs, respectively. The increased prevalence of cells with enhanced heterogeneity in Split and Poly population relative to Normative is highly consistent across experiments. The absolute ratios vary to some extent, but largely mirror the ratio of multi-innervation observed in slice electrophysiology experiments (Fig. 2D) and reflect an expected relationship in which spontaneous activity, as in A, is more likely to be affected by unsynchronized climbing fiber signaling than sensory evoked conditions, as in B and C. Among evoked conditions, climbing fiber signaling is most likely to be highly synchronized, reducing the ability to observe multi-innervation, during awake responses to multi-sensory stimuli.

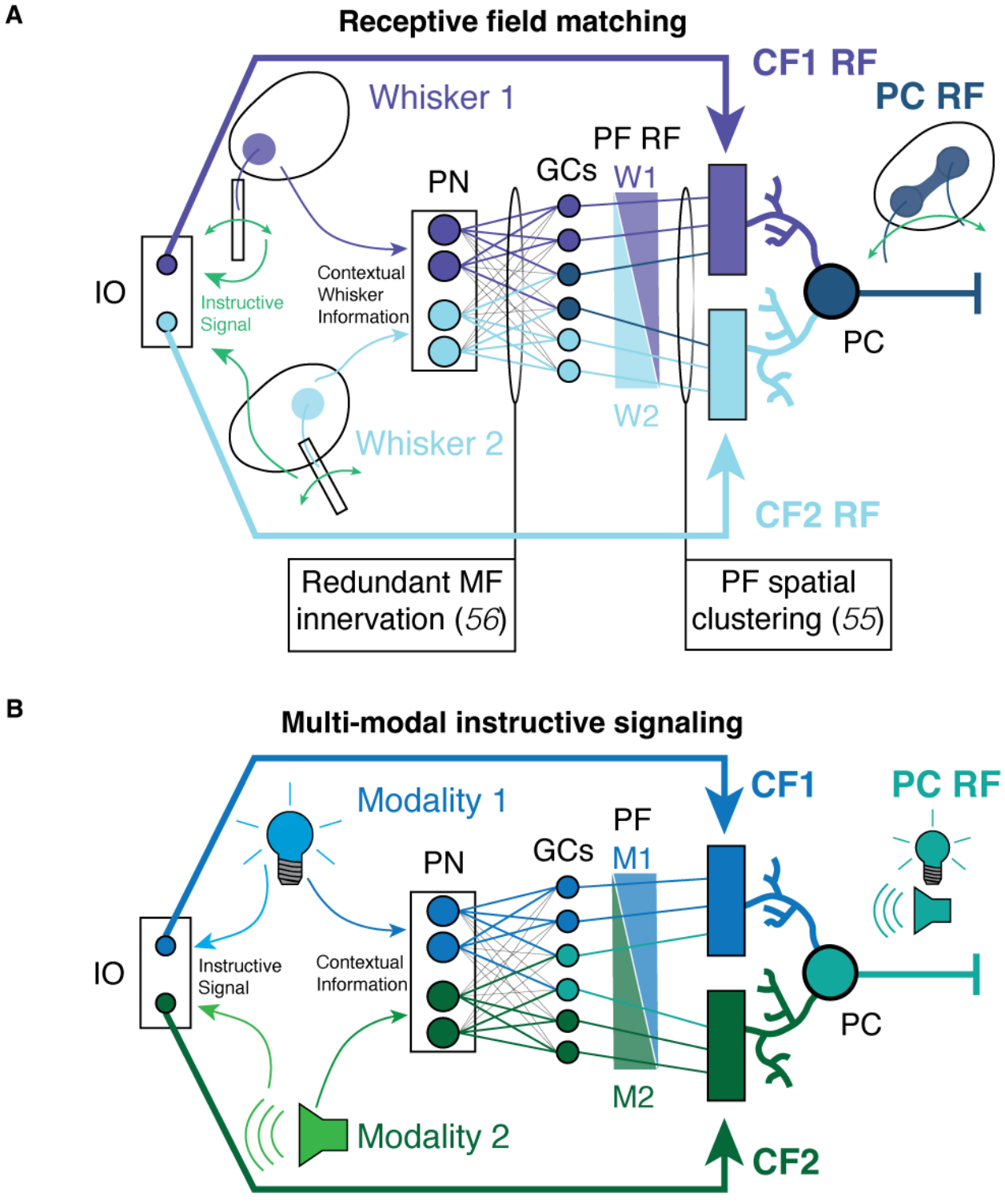
A
Receptive field matching
CF1 RF
PC RF
Whisker 1
PF RF
PN
GCs
W1
IO
Contextual
Whisker
Information
Instructive
Signal
PC
W2
Whisker 2
CF2 RF
Redundant MF
innervation (56)
PF spatial
clustering (55)
B
Multi-modal instructive signaling
CF1
PC RF
Modality 1
PF
PN
GCs
M1
IO
Instructive
Signal
Contextual
Information
PC
M2
Modality 2
CF2

Fig. S11. Perceptron circuit diagram highlighting the advantage of climbing fiber multi-innervation for polydendritic Purkinje cells. (**A**) A cerebellar circuit diagram with a two-layer perceptron network model representing the supervised associative learning function of a Purkinje cell (PC) during exposure to perturbations within the same modality but with distinct receptive fields. The increased dendritic complexity of Split and Poly Purkinje cells – with the addition of parasagittally segregated primary dendrite compartments – within a cortical architecture with functional clustering of upstream projections (55-56) – may increase the range of parallel fiber (PF) receptive field (RF) representation across opposing branches. In a classical perceptron model of the Purkinje cell, a hidden layer of granule cell (GC) parallel fibers (PF) has full connectivity with a single PC dendritic compartment. PF synaptic weights are updated during supervised learning by the instructive signal of a single climbing fiber (CF). Avoiding inappropriate correction of weights requires RF matching between instructor and instructee; the CF RF should thus match that of the PF input population. In some cases, the segregation of PF RFs to different primary dendrites may necessitate distinct CF inputs to retain RF-matching. The diagram in A demonstrates RF matching of the CF instructive signal with the propagation of the mossy fiber (MF) input layer RF through the GC hidden layer to a two compartment PC output layer. A consequence of this arrangement is that signals from the output layer generalize across RFs of the PF and CF inputs. (**B**) A second advantage of CF multi-innervation is the potential use for representation of error / instructive signals from multi-modal sensory environments. IO = inferior olive, PN = pontine nucleus

Lobule*	H2†						H3‡						H4§					
	N		S		P		N		S		P		N		S		P	
	n	%	n	%	n	%	n	%	n	%	n	%	n	%	n	%	n	%
L3													5	29	8	47	4	24
L4													14	16	56	65	16	19
L5	34	4	394	47	410	49	18	8	128	56	84	37	11	6	133	72	40	22
L6	18	4	153	38	236	58	10	4	146	57	100	39	7	4	86	54	65	41
L7Af/Crus1	25	3	297	38	460	59	17	4	207	43	255	53	12	4	129	44	150	52
L7At/Crus2	32	5	326	47	332	48	12	5	100	38	151	57	10	2	236	48	250	50
L7B	9	5	79	40	111	56	11	3	125	36	214	61	7	3	106	50	101	47
L8A	6	3	77	40	108	57	7	2	102	36	175	62						
L8B			9	69	4	31	3	1	80	37	135	62						

**Lobules present in each individual differ with variations in slicing and tissue quality.*

†92yo, Female, Cause of Death: 'Failure to Thrive'

‡95yo, Female, Cause of Death: 'Failure to Thrive'

§86yo, Male, Cause of Death: 'Colon Cancer'

Table S1. Distribution of PC morphologies in human.

Lobule specific numbers and percentages (in color) of each morphological type for each individual in the study. Lobule information is empty if the lobule was not present or could not be assessed in sections from that individual. Related to Figure 1B-C, and fig S2.

Lobule	Mse1						Mse2						Mse3					
	N		S		P		N		S		P		N		S		P	
	n	%	n	%	n	%	n	%	n	%	n	%	n	%	n	%	n	%
L2	19	46	17	41	5	12	29	69	9	21	4	10	27	66	9	22	5	12
L3	42	66	16	25	6	9	22	67	8	24	3	9	15	58	10	38	1	4
L4	23	46	24	48	3	6	19	58	12	36	2	6	16	52	15	48	0	0
L5	22	45	18	37	9	18	23	45	21	41	7	14	22	51	14	33	7	16
L6	30	49	29	48	2	3	33	66	11	22	6	12	30	47	26	41	8	12
L7Af/Crus1	5	42	6	50	1	8	5	33	5	33	5	33	5	42	6	50	1	8
L7At/Crus2	15	31	25	52	8	17	12	36	16	48	5	15	9	31	13	45	7	24
L8A	18	51	14	40	3	9	11	42	14	54	1	4	13	34	11	29	14	37
L8B	17	45	11	29	10	26	5	28	6	33	7	39	6	29	2	10	13	62
L9	54	47	26	23	35	30	26	42	21	34	15	24	25	33	32	42	19	25
L10	12	44	13	48	2	7	17	53	10	31	5	16	14	41	15	44	5	15

Table S2. Distribution of PC morphologies in mouse.

Lobule specific numbers and percentages (in color) of each morphological type for each mouse in this experiment. Related to Figure 1E-F.

	Normative M	Normative H	Split M	Split H	Poly M
Normative H	<0.001				
Split M	<0.001	<0.001			
Split H	1	<0.001	<0.001		
Poly M	<0.001	<0.001	<0.001	<0.001	
Poly H	0.218	<0.001	<0.001	<0.001	<0.001

	Normative M	Normative H	Split M	Split H	Poly M
Normative H	0.512				
Split M	0.116	0.408			
Split H	0.020	0.474	0.067		
Poly M	0.330	0.195	0.219	0.215	
Poly H	0.027	0.527	0.114	0.064	0.260

Table S3. Morphology demographics by species.

Quantification of p-values (top) and φ effect size (bottom) after a multiple comparisons Z-test of proportions with post-hoc bonferroni correction of morphological demographics by species. Related to Figure 1G. M = Mouse; H = Human.

	Anterior M Normative	Anterior H Normative	Posterior M Normative	Posterior H Normative	Anterior M Split	Anterior H Split	Posterior M Split	Posterior H Split	Anterior M Poly	Anterior H Poly	Posterior M Poly
Anterior H Normative	<0.001										
Posterior M Normative	<0.001	<0.001									
Posterior H Normative	<0.001	<0.001	<0.001								
Anterior M Split	<0.001	<0.001	0.0002	<0.001							
Anterior H Split	<0.001	<0.001	<0.001	<0.001	<0.001						
Posterior M Split	<0.001	<0.001	1	<0.001	<0.001	<0.001					
Posterior H Split	<0.001	<0.001	<0.001	<0.001	0.022	<0.001	<0.001				
Anterior M Poly	<0.001	1	<0.001	<0.001	<0.001	<0.001	0.0001	<0.001			
Anterior H Poly	<0.001	<0.001	<0.001	<0.001	<0.001	<0.001	<0.001	<0.001	<0.001		
Posterior M Poly	<0.001	1	<0.001	<0.001	<0.001	<0.001	<0.001	<0.001	1	<0.001	
Posterior H Poly	1	<0.001	<0.001	<0.001	<0.001	<0.001	<0.001	<0.001	<0.001	<0.001	<0.001

	Anterior M Normative	Anterior H Normative	Posterior M Normative	Posterior H Normative	Anterior M Split	Anterior H Split	Posterior M Split	Posterior H Split	Anterior M Poly	Anterior H Poly	Posterior M Poly
Anterior H Normative	0.480										
Posterior M Normative	0.301	0.153									
Posterior H Normative	0.537	0.117	0.304								
Anterior M Split	0.209	0.284	0.107	0.359							
Anterior H Split	0.484	0.846	0.689	0.851	0.659						
Posterior M Split	0.340	0.118	0.039	0.264	0.145	0.722					
Posterior H Split	0.071	0.215	0.158	0.464	0.047	0.348	0.186				
Anterior M Poly	0.477	0.006	0.146	0.095	0.286	0.855	0.114	0.186			
Anterior H Poly	0.187	0.633	0.486	0.705	0.388	0.301	0.522	0.204	0.619		
Posterior M Poly	0.454	0.012	0.153	0.150	0.259	0.812	0.114	0.258	0.019	0.624	
Posterior H Poly	0.008	0.283	0.244	0.556	0.109	0.279	0.271	0.111	0.244	0.131	0.340

Table S4. Morphology demographics by cerebellar region and species.

Quantification of p-values (top) and φ effect size (bottom) after a multiple comparisons Z-test of proportions with post-hoc bonferroni correction of morphological demographics by cerebellar region and species. M = Mouse; H = Human; A = Anterior lobules (L2-L5); P = Posterior lobules (L6-L10). Related to Figure 1G and fig S2A.

	Z+ N	Z+ S/P	Z- N
Z+ S/P	1		
Z- N	0.046	0.004	
Z- S/P	0.004	0.0001	1

	Z+ N	Z+ S/P	Z- N
Z+ S/P	0.013		
Z- N	0.255	0.276	
Z- S/P	0.276	0.316	0.013

Table S5. No relationship between zebrin II expression and Purkinje morphology in the mouse. Quantification of p-values (top) and φ effect size (bottom) after multiple comparisons Z-test of proportions with post-hoc bonferroni correction of morphological demographics by zebrin expression. Related to fig S3B.

	N Z+	N Z-	S/P Z+
N Z-	0.147		
S/P Z+	0	0	
S/P Z-	0	0	0.147

	N Z+	N Z-	S/P Z+
N Z-	0.177		
S/P Z+	0.960	0.858	
S/P Z-	0.858	0.759	0.177

Table S6. No relationship between zebrin II expression and Purkinje morphology in the mouse. Quantification of p-values (top) and φ effect size (bottom) after multiple comparisons Z-test of proportions with post-hoc bonferroni correction of morphological demographics by zebrin expression. Related to fig S3E.

	Normative Gyrus	Normative Bank	Normative Sulcus	Split Gyrus	Split Bank	Split Sulcus	Poly Gyrus	Poly Bank
Normative Bank	1							
Normative Sulcus	1	0.121						
Split Gyrus	1	0.001	1					
Split Bank	0.020	<0.001	1	1				
Split Sulcus	1	1	1	1	1			
Poly Gyrus	<0.001	<0.001	<0.001	<0.001	<0.001	<0.001		
Poly Bank	<0.001	<0.001	<0.001	<0.001	<0.001	<0.001	1	
Poly Sulcus	<0.001	<0.001	0.001	0.0005	0.005	0.0001	1	1

	Normative Gyrus	Normative Bank	Normative Sulcus	Split Gyrus	Split Bank	Split Sulcus	Poly Gyrus	Poly Bank
Normative Bank	0.058							
Normative Sulcus	0.050	0.093						
Split Gyrus	0.067	0.122	0.009					
Split Bank	0.101	0.173	0.040	0.036				
Split Sulcus	0.020	0.069	0.026	0.039	0.066			
Poly Gyrus	0.283	0.310	0.225	0.216	0.159	0.255		
Poly Bank	0.312	0.377	0.230	0.245	0.212	0.258	0.030	
Poly Sulcus	0.248	0.251	0.211	0.185	0.122	0.242	0.010	0.038

Table S7. Morphology demographics by foliar sub-region in the mouse. Quantification of p-values (top) and φ effect size (bottom) after a multiple comparisons Z-test of proportions with post-hoc bonferroni correction of morphological demographics by cerebellar sub-region (e.g. Gyrus, Bank, and Sulcus). Related to fig S4C (left).

	Normative Gyrus	Normative Bank	Normative Sulcus	Split Gyrus	Split Bank	Split Sulcus	Poly Gyrus	Poly Bank
Normative Bank	1							
Normative Sulcus	<0.001	<0.001						
Split Gyrus	<0.001	<0.001	<0.001					
Split Bank	<0.001	<0.001	<0.001	0.118				
Split Sulcus	<0.001	<0.001	<0.001	0.015	1			
Poly Gyrus	<0.001	<0.001	<0.001	<0.001	<0.001	0.001		
Poly Bank	<0.001	<0.001	<0.001	0.00000	0.104	1	0.132	
Poly Sulcus	<0.001	<0.001	<0.001	<0.001	0.0004	0.072	1	1

	Normative Gyrus	Normative Bank	Normative Sulcus	Split Gyrus	Split Bank	Split Sulcus	Poly Gyrus	Poly Bank
Normative Bank	0							
Normative Sulcus	0.112	0.101						
Split Gyrus	0.423	0.446	0.500					
Split Bank	0.413	0.463	0.480	0.043				
Split Sulcus	0.461	0.494	0.533	0.059	0.013			
Poly Gyrus	0.532	0.558	0.603	0.128	0.079	0.069		
Poly Bank	0.444	0.495	0.510	0.080	0.038	0.024	0.043	
Poly Sulcus	0.503	0.537	0.572	0.108	0.062	0.049	0.019	0.024

Table S8. Morphology demographics by foliar sub-region in the human. Quantification of p-values (top) and φ effect size (bottom) after a multiple comparisons Z-test of proportions with post-hoc bonferroni correction of morphological demographics by cerebellar sub-region (e.g. Gyrus, Bank, and Sulcus). Related to fig S4C (right).

	Normative Gyrus	Normative Bank	Normative Sulcus	Vertical S/P Gyrus	Vertical S/P Bank	Vertical S/P Sulcus	Horizontal S/P Gyrus	Horizontal S/P Bank
Normative Bank	1							
Normative Sulcus	1	0.121						
Vertical S/P Gyrus	1	1	1					
Vertical S/P Bank	1	0.659	1	1				
Vertical S/P Sulcus	1	1	0.285	1	1			
Horizontal S/P Gyrus	<0.001	<0.001	<0.001	<0.001	<0.001	<0.001		
Horizontal S/P Bank	<0.001	<0.001	<0.001	<0.001	<0.001	<0.001	0.224	
Horizontal S/P Sulcus	<0.001	<0.001	<0.001	<0.001	<0.001	<0.001	1	1

	Normative Gyrus	Normative Bank	Normative Sulcus	Vertical S/P Gyrus	Vertical S/P Bank	Vertical S/P Sulcus	Horizontal S/P Gyrus	Horizontal S/P Bank
Normative Bank	0.058							
Normative Sulcus	0.050	0.093						
Vertical S/P Gyrus	0.025	0.033	0.077					
Vertical S/P Bank	0.002	0.059	0.046	0.020				
Vertical S/P Sulcus	0.076	0.013	0.135	0.050	0.061			
Horizontal S/P Gyrus	0.407	0.406	0.367	0.432	0.358	0.494		
Horizontal S/P Bank	0.498	0.522	0.437	0.522	0.472	0.558	0.080	
Horizontal S/P Sulcus	0.366	0.339	0.354	0.388	0.297	0.478	0	0.070

Table S9. Dendrite orientation by foliar sub-region in the mouse. Quantification of p-values (top) and φ effect size (bottom) after a multiple comparisons Z-test of proportions with post-hoc bonferroni correction of dendrite orientation demographics (e.g. Vertical v.s. Horizontal) among Split and Poly PCs by cerebellar sub-region (e.g. Gyrus, Bank, and Sulcus). Related to fig S4D (left).

	Normative Gyrus	Normative Bank	Normative Sulcus	Vertical S/P Gyrus	Vertical S/P Bank	Vertical S/P Sulcus	Horizontal S/P Gyrus	Horizontal S/P Bank
Normative Bank	1							
Normative Sulcus	<0.001	<0.001						
Vertical S/P Gyrus	<0.001	<0.001	<0.001					
Vertical S/P Bank	<0.001	<0.001	<0.001	1				
Vertical S/P Sulcus	<0.001	<0.001	<0.001	<0.001	<0.001			
Horizontal S/P Gyrus	<0.001	<0.001	<0.001	<0.001	<0.001	0.155		
Horizontal S/P Bank	<0.001	<0.001	<0.001	<0.001	<0.001	1	1	
Horizontal S/P Sulcus	<0.001	<0.001	<0.001	0.00000	0.0001	<0.001	<0.001	<0.001

	Normative Gyrus	Normative Bank	Normative Sulcus	Vertical S/P Gyrus	Vertical S/P Bank	Vertical S/P Sulcus	Horizontal S/P Gyrus	Horizontal S/P Bank
Normative Bank	0							
Normative Sulcus	0.112	0.101						
Vertical S/P Gyrus	0.678	0.698	0.739					
Vertical S/P Bank	0.648	0.697	0.706	0.022				
Vertical S/P Sulcus	0.212	0.227	0.300	0.517	0.523			
Horizontal S/P Gyrus	0.262	0.274	0.350	0.475	0.476	0.048		
Horizontal S/P Bank	0.213	0.240	0.289	0.484	0.517	0.022	0.024	
Horizontal S/P Sulcus	0.737	0.760	0.793	0.091	0.065	0.593	0.553	0.565

Table S10. Dendrite orientation by foliar sub-region in the human. Quantification of p-values (top) and φ effect size (bottom) after a multiple comparisons Z-test of proportions with post-hoc bonferroni correction of dendrite orientation demographics (e.g. Vertical v.s. Horizontal) among Split and Poly PCs by cerebellar sub-region (e.g. Gyrus, Bank, and Sulcus). Related to fig S4D (right).

Movie S1. Sample video of spontaneous calcium signal heterogeneity.

An example of sparse expression of GCaMP6f yielding a lone Purkinje cell in the mouse. Individual branches exhibit global events as well as events that are local to either one branch or the other. Video playback speed is reduced to 0.5x speed.

References and Notes

1. R. Apps, R. Hawkes, Cerebellar cortical organization: A one-map hypothesis. *Nat. Rev. Neurosci.* **10**, 670–681 (2009). doi:10.1038/nrn2698 Medline

2. H. Nedelescu, M. Abdelhack, A. T. Pritchard, Regional differences in Purkinje cell morphology in the cerebellar vermis of male mice. *J. Neurosci. Res.* **96**, 1476–1489 (2018). doi:10.1002/jnr.24206 Medline

3. C. Golgi, *Sulla fina anatomia del cervelletto umano* (Archivio Italiano per le Malattie Nervose, 1874), vol. 2.

4. S. Ramón y Cajal, *Histologie du système nerveux de l'homme and des vertébrés* (Paris : Maloine, 1909).

5. T. Kato, A. Hirano, J. F. Llena, A Golgi study of the human Purkinje cell soma and dendrites. *Acta Neuropathol.* **68**, 145–148 (1985). doi:10.1007/BF00688636 Medline

6. E. D. Louis, M. Lee, R. Babij, K. Ma, E. Cortés, J.-P. G. Vonsattel, P. L. Faust, Reduced Purkinje cell dendritic arborization and loss of dendritic spines in essential tremor. *Brain* **137**, 3142–3148 (2014). doi:10.1093/brain/awu314 Medline

7. J. C. Eccles, M. Ito, J. Szentágothai, *The Cerebellum as a Neuronal Machine* (Springer, 1967).

8. K. Hashimoto, M. Kano, Functional differentiation of multiple climbing fiber inputs during synapse elimination in the developing cerebellum. *Neuron* **38**, 785–796 (2003). doi:10.1016/S0896-6273(03)00298-8 Medline

9. K. Hashimoto, R. Ichikawa, K. Kitamura, M. Watanabe, M. Kano, Translocation of a "winner" climbing fiber to the Purkinje cell dendrite and subsequent elimination of "losers" from the soma in developing cerebellum. *Neuron* **63**, 106–118 (2009). doi:10.1016/j.neuron.2009.06.008 Medline

10. A. M. Wilson, R. Schalek, A. Suissa-Peleg, T. R. Jones, S. Knowles-Barley, H. Pfister, J. W. Lichtman, Developmental Rewiring between Cerebellar Climbing Fibers and Purkinje Cells Begins with Positive Feedback Synapse Addition. *Cell Rep.* **29**, 2849–2861.e6 (2019). doi:10.1016/j.celrep.2019.10.081 Medline

11. C. Hansel, D. J. Linden, Long-term depression of the cerebellar climbing fiber—Purkinje neuron synapse. *Neuron* **26**, 473–482 (2000). doi:10.1016/S0896-6273(00)81179-4 Medline

12. L. W. J. Bosman, H. Takechi, J. Hartmann, J. Eilers, A. Konnerth, Homosynaptic long-term synaptic potentiation of the "winner" climbing fiber synapse in developing Purkinje cells. *J. Neurosci.* **28**, 798–807 (2008). doi:10.1523/JNEUROSCI.4074-07.2008 Medline

13. G. Ohtsuki, T. Hirano, Bidirectional plasticity at developing climbing fiber-Purkinje neuron synapses. *Eur. J. Neurosci.* **28**, 2393–2400 (2008). doi:10.1111/j.1460-9568.2008.06539.x Medline

14. C. Piochon, M. Kano, C. Hansel, LTD-like molecular pathways in developmental synaptic pruning. *Nat. Neurosci.* **19**, 1299–1310 (2016). doi:10.1038/nn.4389 Medline

15. N. L. Cerminara, E. J. Lang, R. V. Sillitoe, R. Apps, Redefining the cerebellar cortex as an assembly of non-uniform Purkinje cell microcircuits. *Nat. Rev. Neurosci.* **16**, 79–93 (2015). doi:10.1038/nrn3886 Medline

16. J. C. Eccles, R. Llinás, K. Sasaki, The excitatory synaptic action of climbing fibres on the Purkinje cells of the cerebellum. *J. Physiol.* **182**, 268–296 (1966). doi:10.1113/jphysiol.1966.sp007824 Medline

17. J. I. Simpson, D. Wylie, C. I. De Zeeuw, On climbing fiber signals and their consequence(s). *Behav. Brain Sci.* **19**, 384–398 (1996). doi:10.1017/S0140525X00081486

18. A. Badura, M. Schonewille, K. Voges, E. Galliano, N. Renier, Z. Gao, L. Witter, F. E. Hoebeek, A. Chédotal, C. I. De Zeeuw, Climbing fiber input shapes reciprocity of Purkinje cell firing. *Neuron* **78**, 700–713 (2013). doi:10.1016/j.neuron.2013.03.018 Medline

19. M. Ito, M. Sakurai, P. Tongroach, Climbing fibre induced depression of both mossy fibre responsiveness and glutamate sensitivity of cerebellar Purkinje cells. *J. Physiol.* **324**, 113–134 (1982). doi:10.1113/jphysiol.1982.sp014103 Medline

20. S. S.-H. Wang, W. Denk, M. Häusser, Coincidence detection in single dendritic spines mediated by calcium release. *Nat. Neurosci.* **3**, 1266–1273 (2000). doi:10.1038/81792 Medline

21. V. Lev-Ram, S. T. Wong, D. R. Storm, R. Y. Tsien, A new form of cerebellar long-term potentiation is postsynaptic and depends on nitric oxide but not cAMP. *Proc. Natl. Acad. Sci. U.S.A.* **99**, 8389–8393 (2002). doi:10.1073/pnas.122206399 Medline

22. J. F. Medina, W. L. Nores, M. D. Mauk, Inhibition of climbing fibres is a signal for the extinction of conditioned eyelid responses. *Nature* **416**, 330–333 (2002). doi:10.1038/416330a Medline

23. M. Coesmans, J. T. Weber, C. I. De Zeeuw, C. Hansel, Bidirectional parallel fiber plasticity in the cerebellum under climbing fiber control. *Neuron* **44**, 691–700 (2004). doi:10.1016/j.neuron.2004.10.031 Medline

24. C. Piochon, H. K. Titley, D. H. Simmons, G. Grasselli, Y. Elgersma, C. Hansel, Calcium threshold shift enables frequency-independent control of plasticity by an instructive signal. *Proc. Natl. Acad. Sci. U.S.A.* **113**, 13221–13226 (2016). doi:10.1073/pnas.1613897113 Medline

25. M. L. Streng, L. S. Popa, T. J. Ebner, Climbing Fibers Control Purkinje Cell Representations of Behavior. *J. Neurosci.* **37**, 1997–2009 (2017). doi:10.1523/JNEUROSCI.3163-16.2017 Medline

26. H. K. Titley, M. Kislin, D. H. Simmons, S. S.-H. Wang, C. Hansel, Complex spike clusters and false-positive rejection in a cerebellar supervised learning rule. *J. Physiol.* **597**, 4387–4406 (2019). doi:10.1113/JP278502 Medline

27. C. Piochon, A. D. Kloth, G. Grasselli, H. K. Titley, H. Nakayama, K. Hashimoto, V. Wan, D. H. Simmons, T. Eissa, J. Nakatani, A. Cherskov, T. Miyazaki, M. Watanabe, T. Takumi, M. Kano, S. S.-H. Wang, C. Hansel, Cerebellar plasticity and motor learning deficits in a copy-number variation mouse model of autism. *Nat. Commun.* **5**, 5586 (2014). doi:10.1038/ncomms6586 Medline

28. M. Kano, K. Hashimoto, H. Kurihara, M. Watanabe, Y. Inoue, A. Aiba, S. Tonegawa, Persistent multiple climbing fiber innervation of cerebellar Purkinje cells in mice lacking mGluR1. *Neuron* **18**, 71–79 (1997). doi:10.1016/S0896-6273(01)80047-7 Medline

29. H. Nishiyama, D. J. Linden, Differential maturation of climbing fiber innervation in cerebellar vermis. *J. Neurosci.* **24**, 3926–3932 (2004). doi:10.1523/JNEUROSCI.5610-03.2004 Medline

30. T. Miyazaki, M. Watanabe, Development of an anatomical technique for visualizing the mode of climbing fiber innervation in Purkinje cells and its application to mutant mice lacking GluRδ2 and Ca(v)2.1. *Anat. Sci. Int.* **86**, 10–18 (2011). doi:10.1007/s12565-010-0095-1 Medline

31. M. Kano, T. Watanabe, N. Uesaka, M. Watanabe, Multiple Phases of Climbing Fiber Synapse Elimination in the Developing Cerebellum. *Cerebellum* **17**, 722–734 (2018). doi:10.1007/s12311-018-0964-z Medline

32. I. Llano, A. Marty, C. M. Armstrong, A. Konnerth, Synaptic- and agonist-induced excitatory currents of Purkinje cells in rat cerebellar slices. *J. Physiol.* **434**, 183–213 (1991). doi:10.1113/jphysiol.1991.sp018465 Medline

33. M. T. Schmolesky, J. T. Weber, C. I. De Zeeuw, C. Hansel, The making of a complex spike: Ionic composition and plasticity. *Ann. N. Y. Acad. Sci.* **978**, 359–390 (2002). doi:10.1111/j.1749-6632.2002.tb07581.x Medline

34. C. Piochon, C. Levenes, G. Ohtsuki, C. Hansel, Purkinje cell NMDA receptors assume a key role in synaptic gain control in the mature cerebellum. *J. Neurosci.* **30**, 15330–15335 (2010). doi:10.1523/JNEUROSCI.4344-10.2010 Medline

35. H. Takechi, J. Eilers, A. Konnerth, A new class of synaptic response involving calcium release in dendritic spines. *Nature* **396**, 757–760 (1998). doi:10.1038/25547 Medline

36. G. Ohtsuki, C. Piochon, J. P. Adelman, C. Hansel, SK2 channel modulation contributes to compartment-specific dendritic plasticity in cerebellar Purkinje cells. *Neuron* **75**, 108–120 (2012). doi:10.1016/j.neuron.2012.05.025 Medline

37. J. C. Callaway, N. Lasser-Ross, W. N. Ross, IPSPs strongly inhibit climbing fiber-activated [Ca2+]i increases in the dendrites of cerebellar Purkinje neurons. *J. Neurosci.* **15**, 2777–2787 (1995). doi:10.1523/JNEUROSCI.15-04-02777.1995 Medline

38. M. J. M. Rowan, A. Bonnan, K. Zhang, S. B. Amat, C. Kikuchi, H. Taniguchi, G. J. Augustine, J. M. Christie, Graded Control of Climbing-Fiber-Mediated Plasticity and Learning by Inhibition in the Cerebellum. *Neuron* **99**, 999–1015.e6 (2018). doi:10.1016/j.neuron.2018.07.024 Medline

39. K. Kitamura, M. Häusser, Dendritic calcium signaling triggered by spontaneous and sensory-evoked climbing fiber input to cerebellar Purkinje cells in vivo. *J. Neurosci.* **31**, 10847–10858 (2011). doi:10.1523/JNEUROSCI.2525-10.2011 Medline

40. Y. Zang, S. Dieudonné, E. De Schutter, Voltage- and Branch-Specific Climbing Fiber Responses in Purkinje Cells. *Cell Rep.* **24**, 1536–1549 (2018). doi:10.1016/j.celrep.2018.07.011 Medline

41. C. J. Roome, B. Kuhn, Simultaneous dendritic voltage and calcium imaging and somatic recording from Purkinje neurons in awake mice. *Nat. Commun.* **9**, 3388 (2018). doi:10.1038/s41467-018-05900-3 Medline

42. F. Najafi, A. Giovannucci, S. S.-H. Wang, J. F. Medina, Sensory-driven enhancement of calcium signals in individual Purkinje cell dendrites of awake mice. *Cell Rep.* **6**, 792–798 (2014). doi:10.1016/j.celrep.2014.02.001 Medline

43. M. A. Gaffield, A. Bonnan, J. M. Christie, Conversion of Graded Presynaptic Climbing Fiber Activity into Graded Postsynaptic Ca^{2+} Signals by Purkinje Cell Dendrites. *Neuron* **102**, 762–769.e4 (2019). doi:10.1016/j.neuron.2019.03.010 Medline

44. S.-E. Roh, S. H. Kim, C. Ryu, C.-E. Kim, Y. G. Kim, P. F. Worley, S. K. Kim, S. J. Kim, Direct translation of climbing fiber burst-mediated sensory coding into post-synaptic Purkinje cell dendritic calcium. *eLife* **9**, e61593 (2020). doi:10.7554/eLife.61593 Medline

45. L. W. J. Bosman, S. K. E. Koekkoek, J. Shapiro, B. F. M. Rijken, F. Zandstra, B. van der Ende, C. B. Owens, J.-W. Potters, J. R. de Gruijl, T. J. H. Ruigrok, C. I. De Zeeuw, Encoding of whisker input by cerebellar Purkinje cells. *J. Physiol.* **588**, 3757–3783 (2010). doi:10.1113/jphysiol.2010.195180 Medline

46. C. Ju, L. W. J. Bosman, T. M. Hoogland, A. Velauthapillai, P. Murugesan, P. Warnaar, R. M. van Genderen, M. Negrello, C. I. De Zeeuw, Neurons of the inferior olive respond to broad classes of sensory input while subject to homeostatic control. *J. Physiol.* **597**, 2483–2514 (2019). doi:10.1113/JP277413 Medline

47. J. Cichon, A. Z. Wasilczuk, L. L. Looger, D. Contreras, M. B. Kelz, A. Proekt, Ketamine triggers a switch in excitatory neuronal activity across neocortex. *Nat. Neurosci.* **26**, 39–52 (2022). doi:10.1038/s41593-022-01203-5 Medline

48. F. Najafi, A. Giovannucci, S. S.-H. Wang, J. F. Medina, Coding of stimulus strength via analog calcium signals in Purkinje cell dendrites of awake mice. *eLife* **3**, e03663 (2014). doi:10.7554/eLife.03663 Medline

49. D. H. Simmons, S. E. Busch, H. K. Titley, G. Grasselli, J. Shih, X. Du, C. Wei, C. M. Gomez, C. Piochon, C. Hansel, Sensory Over-responsivity and Aberrant Plasticity in Cerebellar Cortex in a Mouse Model of Syndromic Autism. *Biol. Psychiatry Glob. Open Sci.* **2**, 450–459 (2021). doi:10.1016/j.bpsgos.2021.09.004 Medline

50. Y. Yang, S. G. Lisberger, Purkinje-cell plasticity and cerebellar motor learning are graded by complex-spike duration. *Nature* **510**, 529–532 (2014). doi:10.1038/nature13282 Medline

51. S. Ohmae, J. F. Medina, Climbing fibers encode a temporal-difference prediction error during cerebellar learning in mice. *Nat. Neurosci.* **18**, 1798–1803 (2015). doi:10.1038/nn.4167 Medline

52. W. Heffley, C. Hull, Classical conditioning drives learned reward prediction signals in climbing fibers across the lateral cerebellum. *eLife* **8**, e46764 (2019). doi:10.7554/eLife.46764 Medline

53. D. Kostadinov, M. Beau, M. Blanco-Pozo, M. Häusser, Predictive and reactive reward signals conveyed by climbing fiber inputs to cerebellar Purkinje cells. *Nat. Neurosci.* **22**, 950–962 (2019). doi:10.1038/s41593-019-0381-8 Medline

54. A. L. Person, I. M. Raman, Purkinje neuron synchrony elicits time-locked spiking in the cerebellar nuclei. *Nature* **481**, 502–505 (2011). doi:10.1038/nature10732 Medline

55. C. D. Wilms, M. Häusser, Reading out a spatiotemporal population code by imaging neighbouring parallel fibre axons in vivo. *Nat. Commun.* **6**, 6464 (2015). doi:10.1038/ncomms7464 Medline

56. T. M. Nguyen, L. A. Thomas, J. L. Rhoades, I. Ricchi, X. C. Yuan, A. Sheridan, D. G. C. Hildebrand, J. Funke, W. G. Regehr, W. A. Lee, Structured cerebellar connectivity supports resilient pattern separation. *Nature* **613**, 543–549 (2023). doi:10.1038/s41586-022-05471-w Medline

57. N. Brunel, V. Hakim, P. Isope, J.-P. Nadal, B. Barbour, Optimal information storage and the distribution of synaptic weights: Perceptron versus Purkinje cell. *Neuron* **43**, 745–757 (2004). Medline

58. C. J. Stoodley, J. D. Schmahmann, Evidence for topographic organization in the cerebellum of motor control versus cognitive and affective processing. *Cortex* **46**, 831–844 (2010). doi:10.1016/j.cortex.2009.11.008 Medline

59. A. Badura, J. L. Verpeut, J. W. Metzger, T. D. Pereira, T. J. Pisano, B. Deverett, D. E. Bakshinskaya, S. S.-H. Wang, Normal cognitive and social development require posterior cerebellar activity. *eLife* **7**, e36401 (2018). doi:10.7554/eLife.36401 Medline

60. A. LeBel, S. Jain, A. G. Huth, Voxelwise Encoding Models Show That Cerebellar Language Representations Are Highly Conceptual. *J. Neurosci.* **41**, 10341–10355 (2021). doi:10.1523/JNEUROSCI.0118-21.2021 Medline

61. M.-K. Pan, Y.-S. Li, S.-B. Wong, C.-L. Ni, Y.-M. Wang, W.-C. Liu, L.-Y. Lu, J.-C. Lee, E. P. Cortes, J.-P. G. Vonsattel, Q. Sun, E. D. Louis, P. L. Faust, S.-H. Kuo, Cerebellar oscillations driven by synaptic pruning deficits of cerebellar climbing fibers contribute to tremor pathophysiology. *Sci. Transl. Med.* **12**, eaay1769 (2020). doi:10.1126/scitranslmed.aay1769 Medline

62. S. Busch, Climbing fiber multi-innervation of mouse Purkinje dendrites with arborization common to human, Dryad (2023); https://doi.org/10.5061/dryad.kh18932c1.

63. F. Lanore, N. A. Cayco-Gajic, H. Gurnani, D. Coyle, R. A. Silver, Cerebellar granule cell axons support high-dimensional representations. *Nat. Neurosci.* **24**, 1142–1150 (2021). doi:10.1038/s41593-021-00873-x Medline

64. T.-W. Chen, T. J. Wardill, Y. Sun, S. R. Pulver, S. L. Renninger, A. Baohan, E. R. Schreiter, R. A. Kerr, M. B. Orger, V. Jayaraman, L. L. Looger, K. Svoboda, D. S. Kim, Ultrasensitive fluorescent proteins for imaging neuronal activity. *Nature* **499**, 295–300 (2013). doi:10.1038/nature12354 Medline

65. M. Kaneko, K. Yamaguchi, M. Eiraku, M. Sato, N. Takata, Y. Kiyohara, M. Mishina, H. Hirase, T. Hashikawa, M. Kengaku, Remodeling of monoplanar Purkinje cell dendrites during cerebellar circuit formation. *PLOS ONE* **6**, e20108 (2011). doi:10.1371/journal.pone.0020108 Medline

66. H. Zhou, Z. Lin, K. Voges, C. Ju, Z. Gao, L. W. J. Bosman, T. J. H. Ruigrok, F. E. Hoebeek, C. I. De Zeeuw, M. Schonewille, Cerebellar modules operate at different frequencies. *eLife* **3**, e02536 (2014). doi:10.7554/eLife.02536 Medline